Title: Matrin 3-dependent neurotoxicity is modified by nucleic acid binding and nucleocytoplasmic localization

Abbreviated title: Determinants of Matrin 3-dependent neurotoxicity

Author list: Ahmed M. Malik[1,2], Roberto A. Miguez[3], Xingli Li[3], Ye-Shih Ho[5], Eva L. Feldman[2,3,4], and Sami J. Barmada*[,2,3]

Affiliations: [1]Medical Scientist Training Program, [2]Neuroscience Graduate Program, [3]Department of Neurology, [4]Program for Neurology Research and Discovery, University of Michigan, Ann Arbor, MI, USA 48104; [5]Institute of Environmental Health Sciences, Wayne State University, Detroit, MI, USA 48201

* To whom correspondence should be addressed:
Sami Barmada
University of Michigan, Department of Neurology
109 Zina Pitcher Place, BSRB 5015
Ann Arbor, MI 48109
sbarmada@umich.edu

ABSTRACT

Abnormalities in nucleic acid processing are associated with the development of amyotrophic lateral sclerosis (ALS) and frontotemporal dementia (FTD). Mutations in *Matrin 3* (*MATR3*), a poorly understood DNA- and RNA-binding protein, cause familial ALS/FTD, and MATR3 pathology is a feature of sporadic disease, suggesting that MATR3 dysfunction is integrally linked to ALS pathogenesis. Using a primary neuron model to assess MATR3-mediated toxicity, we noted that neurons were bidirectionally vulnerable to MATR3 levels, with pathogenic MATR3 mutants displaying enhanced toxicity. MATR3's zinc finger domains partially modulated toxicity, but elimination of its RNA recognition motifs had no effect on neuronal survival, instead facilitating its self-assembly into liquid-like droplets. In contrast to other RNA-binding proteins associated with ALS, cytoplasmic MATR3 redistribution mitigated neurodegeneration, suggesting that nuclear MATR3 mediates toxicity. Our findings offer a foundation for understanding MATR3-related neurodegeneration and how nucleic acid binding functions, localization, and pathogenic mutations drive sporadic and familial disease.

INTRODUCTION

Amyotrophic lateral sclerosis (ALS) is a progressive neurodegenerative disorder resulting in the death of upper and lower motor neurons (Charcot and Joffroy, 1869). Mounting evidence indicates that RNA-binding proteins (RBPs) are integrally involved in the pathogenesis of ALS (Taylor et al., 2016). The majority (>95%) of ALS patients display cytoplasmic mislocalization and deposition of the RBP TDP-43 (TAR DNA/RNA-binding protein of 43 kDa) in affected tissue (Neumann et al., 2006). Moreover, over 40 different ALS-associated mutations have been identified in the gene encoding TDP-43, and mutations in several different RBPs have been similarly linked to familial ALS (Kabashi et al., 2008; Kwiatkowski et al., 2009; Vance et al., 2009; Barmada and Finkbeiner, 2010; Ticozzi et al., 2011; Kim et al., 2013). These mutations often cluster in intrinsically disordered domains that facilitate reversible liquid-liquid phase separation (LLPS), thereby creating ribonucleoprotein granules important for RNA processing, shuttling of mRNAs to sites of local translation, or sequestration of transcripts during stress. Pathogenic mutations in the genes encoding TDP-43 and related RBPs, including FUS and TIA1, shift the equilibrium towards irreversible phase separation and the formation of cytoplasmic aggregates analogous to those observed in post-mortem tissues from patients with ALS (Johnson et al., 2009; Patel et al., 2015; Gopal et al., 2017; Mackenzie et al., 2017). The downstream implications of abnormal LLPS on RNA misprocessing, RBP pathology, and neurodegeneration in ALS are unknown, however.

Matrin 3 (MATR3) is a DNA- and RNA-binding protein with wide-ranging functions in nucleic acid metabolism including gene transcription, the DNA damage response, splicing, RNA degradation, and the sequestration of hyperedited RNAs (Belgrader et al., 1991; Hibino et al., 2000; Zhang and Carmichael, 2001; Salton et al., 2014; Coelho et al., 2015; Rajgor et al., 2016; Uemura et al., 2017). The MATR3 S85C mutation leads to autosomal dominant distal myopathy with vocal cord and pharyngeal

63 weakness (Feit et al., 1998; Senderek et al., 2009). A more recent report reclassified a
64 subset of patients with this diagnosis as having ALS and noted several additional
65 MATR3 mutations in individuals with ALS and frontotemporal dementia (FTD), placing
66 MATR3 in a group of proteins implicated in familial ALS, FTD, and myopathy; other
67 members of this family include VCP, TIA1 and hnRNPA2/B1 (Kimonis et al., 2008;
68 Johnson et al., 2010; Kim et al., 2013; Klar et al., 2013; Johnson et al., 2014; Mackenzie
69 et al., 2017). A total of 13 pathogenic MATR3 mutations have now been identified, most
70 of which are located in disordered stretches of the protein (Fig. 1A) (Millecamps et al.,
71 2014; Origone et al., 2015; Leblond et al., 2016; Xu et al., 2016; Marangi et al., 2017).
72 Additionally, post-mortem analyses demonstrated MATR3 pathology—consisting of
73 cytoplasmic MATR3 accumulation as well as strong nuclear immunostaining—in patients
74 with sporadic ALS and familial disease due to *C9orf72* hexanucleotide expansions and
75 *FUS* mutations (Dreser et al., 2017; Tada et al., 2017).
76 Together, these observations suggest that MATR3 may be a common mediator
77 of disease even in those without *MATR3* mutations. Even so, little is known about
78 MATR3's functions in health or in disease, and the mechanisms underlying MATR3-
79 dependent neurotoxicity remain unclear. Here, we establish an *in vitro* model of MATR3-
80 mediated neurodegeneration and take advantage of this model to investigate the
81 intrinsic properties and domains of MATR3 required for toxicity. Furthermore, we
82 examine how disease-associated MATR3 mutations affect these properties to enhance
83 neurodegeneration.
84
85 **RESULTS**
86 **MATR3 levels modulate neuronal survival in an *in vitro* model of**
87 **neurodegeneration.**
88

We first asked how MATR3 expression is related to neurodegeneration using longitudinal fluorescence microscopy (LFM), a sensitive high-content imaging system that we assembled for assessing neuronal function and survival at the single-cell level. As *MATR3* mutations cause a spectrum of disease that includes ALS and FTD, we modeled neurotoxicity in primary mixed cortical cultures, a system that recapitulates key features of ALS/FTD pathogenesis (Barmada et al., 2010; Barmada et al., 2014; Barmada et al., 2015). Primary neurons were transfected with diffusely localized mApple to enable visualization of neuronal cell bodies and processes by fluorescence microscopy. In addition, cells were co-transfected with constructs encoding enhanced green fluorescent protein (EGFP) or MATR3 fused with EGFP. Cultures were imaged by fluorescence microscopy at 24 h intervals for 10 days, and custom scripts used to generate uniquely labeled regions of interest (ROIs) corresponding to each cell (Fig. 1B). Rounding of the soma, retraction of neurites or loss of fluorescence indicated cell death; these criteria proved to be sensitive markers of neurodegeneration in previous studies (Arrasate and Finkbeiner, 2005). We used the time of death for individual cells to calculate an overall risk of death, expressed as a hazard ratio (HR), corresponding to the likelihood of cell death in each population relative to a control or reference group (Christensen, 1987). In doing so, we observed that MATR3(WT)-EGFP overexpression significantly increases the risk of death compared to EGFP alone, with a HR of 1.48 (Fig. 1C).

Next, we investigated the dose-dependency of this MATR3 toxicity through two alternative but complementary approaches. Transient transfection delivers a different amount of vector to each cell, resulting in substantial variability in protein expression for individual cells. Since fluorescence intensity is directly proportional to fluorophore levels (Arrasate et al., 2004), the GFP intensity within each ROI provides an estimate of EGFP or MATR3(WT)-EGFP expression for individual neurons. Based on the GFP intensity

measured 24 h after transfection, we divided transfected neurons into three groups: those that expressed low, medium, and high levels of EGFP or MATR3(WT)-EGFP. We then assessed the relative survival of these groups over time, and compared the risk of death in each by Cox proportional hazards. In doing so, we noted that cells that express low EGFP levels display an increased risk of death compared to those in the medium or high EGFP expression categories, potentially due to poor protein expression by unhealthy or dying cells (Fig. 1D). We also analyzed the relationship between GFP intensity and survival using penalized splines, which approximate both linear and non-linear relationships by treating GFP intensity as a continuous variable (Miller et al., 2010; Barmada et al., 2015). In this model, increasing EGFP expression predicted improved survival, but the effect plateaued at approximately 1500 arbitrary units (AU) (Fig. 1E). These data imply that lower expression of a neutral protein such as EGFP is tied to reduced survival, consistent with the results of previous studies (Miller et al., 2010; Barmada et al., 2015).

To determine how MATR3(WT)-EGFP expression is related to neuronal survival, we likewise separated neurons into three groups (low, medium and high) depending on MATR3(WT)-EGFP levels and assessed survival in each group. Unlike cells expressing EGFP alone, we detected no significant difference in survival between the low, medium, and high MATR3(WT)-EGFP expression groups (Fig. 1F). Correspondingly, the penalized spline model shows no clear relationship between risk of death and MATR3(WT)-EGFP levels for cells displaying low or medium GFP intensity. However, in contrast to cells expressing EGFP alone, we noted an increase in the risk of death with high MATR3(WT)-EGFP expression (Fig. 1G), suggesting that the extended survival observed in high-expressing cells is offset by the production of a toxic protein. Taken together, these data support a dose-dependent toxicity of MATR3(WT) in primary neurons.

Several *MATR3* mutations have been associated with familial ALS, FTD, and hereditary distal myopathy (Senderek et al., 2009; Johnson et al., 2014; Millecamps et al., 2014; Origone et al., 2015; Leblond et al., 2016; Xu et al., 2016; Marangi et al., 2017). To determine if disease-associated *MATR3* mutations accentuate neurodegeneration, we created MATR3-EGFP fusion proteins harboring one of four mutations originally implicated in familial disease: S85C, F115C, P154S, and T622A (Fig. 1A). Primary rodent cortical neurons expressing these mutant MATR3-EGFP constructs exhibited the same granular nuclear distribution as MATR3(WT)-EGFP, without obvious aggregation or cytoplasmic mislocalization, consistent with prior reports (Fig. 2A) (Gallego-Iradi et al., 2015; Boehringer et al., 2017). Even so, all four displayed a subtle but significant increase in toxicity over MATR3(WT)-EGFP when overexpressed in primary neurons (Fig. 2B), consistent with either gain-of-function or dominant negative loss-of-function mechanisms contributing to mutant MATR3-associated neurodegeneration.

To determine if loss of endogenous MATR3 function is sufficient for neurodegeneration, we transfected primary neurons with mApple and siRNA targeting the amino (N)-terminal coding region of rodent *Matr3* or a scrambled siRNA control. Three days after transfection, Matr3 immunoreactivity was used to quantify efficacy of knockdown in transfected cells (Fig. 2C). Compared to scrambled siRNA-transfected cells, we noted consistent depletion of the endogenous rat Matr3 by approximately 65% in those transfected with siRNA targeting *Matr3* (Fig. 2D). Having confirmed knockdown, we imaged a separate set of transfected cells for 10 days to assess the effect of *Matr3* knockdown on neuronal survival. In doing so, we observed a 20% increase in the risk of death upon *Matr3* depletion in comparison to scrambled siRNA (Fig. 2E). These data suggest that neurons are vulnerable to both increases and decreases in MATR3 levels

and function; further, pathogenic *MATR3* mutations may elicit neurodegeneration via gain- or loss-of-function mechanisms, or through elements of both.

MATR3's zinc finger domains modulate overexpression toxicity, but its RNA recognition motifs mediate self-association.

To identify the functional domains involved in MATR3-mediated neurodegeneration, we systematically deleted each of the annotated MATR3 domains and evaluated subsequent toxicity upon overexpression in primary neurons (Fig. 3A). MATR3 has two zinc-finger (ZF) domains of the C2H2 variety, which bind DNA but may also recognize RNA and/or mediate protein-protein interactions (Brayer et al., 2008; Burdach et al., 2012). Deletions of ZF1, ZF2, or both had no observable effect on MATR3-EGFP localization (Fig. 3B), and ZF1 deletion by itself did not significantly alter toxicity compared to full-length MATR3-EGFP. In contrast, ZF2 deletion, either in isolation or combined with ZF1 deletion, partially rescued MATR3-EGFP overexpression toxicity (Fig. 3C).

We next created deletion variants of MATR3's RNA recognition motifs (RRMs) to test their contribution to MATR3-mediated neurodegeneration. As with the MATR3 ZF domains, RRMs are capable of recognizing both RNA and DNA (Inagaki et al., 1996). While deletion of RRM1 failed to affect MATR3-EGFP localization, we noted a striking redistribution of MATR3(dRRM2)-EGFP into intranuclear granules in a subset of transfected neurons (Fig. 3D). Deletion of RRM1 in combination with RRM2 produced the same phenotype, suggesting that RRM2 normally prevents such redistribution. These nuclear granules formed by MATR3(dRRM2)-EGFP and MATR3(dRRM1/2)-EGFP were uniformly spherical in shape, and their presence was accompanied by a reduction in the intensity of diffusely-distributed MATR3 within the nucleus, suggesting

that they represent hyperconcentrated MATR3 puncta. Evidence from previous studies indicates that RNA recognition by MATR3 may be largely—but not solely—driven by RRM2 (Hibino et al., 2006; Salton et al., 2011). Consistent with this, our finding that RRM2 deletion induces the formation of nuclear condensates suggests that RNA binding normally keeps MATR3 diffuse by preventing an intrinsic tendency for self-association. Despite the dramatic shift in MATR3-EGFP distribution with RRM2 deletion, there was no associated change in the toxicity of MATR3-EGFP lacking RRM1, RRM2 or both in comparison to MATR3(WT)-EGFP (Fig. 3E). This finding stands in contrast to what has been observed for other ALS/FTD-associated RBPs, in which the ability to bind RNAs is a key mediator of overexpression toxicity.

The toxicity of RNA binding-deficient MATR3 variants is highly dependent on their subcellular distribution

One of the hallmarks of neurodegenerative diseases, including ALS and FTD, is the formation of protein-rich aggregates (Arai et al., 2006; Neumann et al., 2006). Prior investigations suggest that these aggregates may be toxic, innocuous, or representative of a coping response that ultimately prolongs neuronal survival (Arrasate et al., 2004; Barmada et al., 2010). To determine if the formation of nuclear puncta by MATR3(dRRM2)-EGFP and MATR3(dRRM1/2)-EGFP affected neuronal lifespan, we turned to LFM. We employed a modified version of the automated analysis script to draw ROIs around the nuclear perimeter within each transfected cell (Fig. 4A) and then calculated a coefficient of variation (CV) for the MATR3(dRRM1/2)-EGFP signal within each nuclear ROI. The CV, or the ratio of the standard deviation of GFP intensity to the mean GFP intensity for the ROI, is directly proportional to the spatial variability of fluorescence intensity within each ROI. Therefore, we reasoned that this measure might

be useful for rapidly and reliably identifying puncta in an unbiased and high-throughput manner. We first validated the use of CV for detecting puncta by creating a receiver-operator characteristic (ROC) curve; in doing so, we observed that a CV threshold of 0.92 was 87.2% sensitive and 93.9% specific in discriminating cells with nuclear granules from those with diffuse protein (Fig. 4B). We therefore utilized this CV threshold to assess the frequency of nuclear granule formation in primary rodent cortical neurons, noting that 24 h after transfection, 23.4% (653/2734) of neurons transfected with MATR3(dRRM2)-EGFP neurons displayed nuclear granules compared to only 8.8% (153/1743) of MATR3(dRRM1/2)-EGFP cells (Fig. 4C). We also observed the time-dependent formation of nuclear granules as neurons expressed increasing amounts of MATR3-EGFP (Fig. 4D), suggesting that granule formation may be proportional to expression level. To investigate this relationship further, we identified neurons exhibiting a diffuse distribution of MATR3(dRRM2)-EGFP at day 1 and followed these cells for an additional 3 days by automated microscopy. We then measured the GFP intensity for each cell at day 1, and related this value to the risk of granule formation over the ensuring 72 h period using penalized splines models. Notably, we failed to observe a significant relationship between GFP intensity on day 1 and granule formation by day 3 (Fig. 3E). We also assessed the relative change in expression level on a per-cell basis, as quantified by the ratio of GFP intensity at day 2 to the GFP intensity at day 1, to determine if the net rate of MATR3(dRRM2)-EGFP production better predicted granule formation. The probability of granule formation was directly proportional to the time-dependent change in MATR3(dRRM2)-EGFP levels (Fig. 4F), suggesting that granule formation is favored by the rapid accumulation of MATR3(dRRM2)-EGFP.

Our previous studies demonstrated that deletion of RRM1 or RRM1 and 2 had no effect upon the toxicity of MATR3-EGFP when expressed in primary neurons (Fig. 3E). These analyses included all neurons within a given condition, consisting of cells with

diffuse nuclear MATR3 as well as those with MATR3 redistributed into granules. To determine if the presence of nuclear MATR3-EGFP granules impacted the survival of neurons, we utilized the nuclear CV threshold (Fig. 4B) to divide neurons expressing MATR3(dRRM2)-EGFP and MATR3(dRRM1/2)-EGFP into three categories: cells with diffuse protein at day 1, those with granules at day 1, or all cells. We then tracked neurons in each category for the following 9 days by LFM, and compared their survival by Cox proportional hazards analysis. By these measures, neurons displaying nuclear MATR3(dRRM2)-EGFP granules fared significantly better than the population as a whole, while those exhibiting a diffuse distribution demonstrated an increased risk of death (Fig. 4G). Similar results were obtained for neurons expressing MATR3(dRRM1/2)-EGFP; here, the relative protection associated with nuclear MATR3(dRRM1/2)-EGFP granules was modest, but the toxicity of diffusely-distributed MATR3(dRRM1/2)-EGFP was more pronounced (Fig. 4H). The marked toxicity of diffuse MATR3(dRRM1/2)-EGFP may explain why so few cells with diffuse protein are seen at day 1 (Fig. 4D). Taken together, these results suggest that diffuse MATR3 is highly neurotoxic when it cannot bind RNA. Furthermore, the sequestration of RNA binding-deficit MATR3 variants into nuclear granules is associated with a survival advantage.

MATR3 granules formed by deletion of the RNA-binding domains display liquid-like properties that are affected by pathogenic mutations

As part of their normal function, many RBPs reversibly undergo liquid-liquid phase separation (LLPS), involving the formation of droplets with liquid-like properties from diffuse or soluble proteins (Molliex et al., 2015; Murray et al., 2017). Disease-associated mutations in the genes encoding these proteins may promote LLPS or impair the reversibility of phase separation (Molliex et al., 2015; Patel et al., 2015; Conicella et

al., 2016). We wondered whether the intranuclear granules formed by MATR3(dRRM2)-EGFP and MATR3(dRRM1/2)-EGFP represent liquid droplets and also whether pathogenic MATR3 mutations affect the intrinsic properties of these puncta. Indeed, nuclear granules exhibited dynamic properties, not only growing in size over time but also moving freely within the nucleus and fusing if they encountered other granules (Fig. 5A), indicative of liquid-like behavior.

We then asked if these structures displayed internal rearrangement characteristic of liquid droplets (Lin et al., 2015; Shin and Brangwynne, 2017) and whether pathogenic *MATR3* mutations affect their dynamics. To answer this, we introduced disease-associated mutations into MATR3(dRRM1/2)-EGFP, and transfected rodent primary cortical neurons with each construct (Fig. 5B). Nuclear puncta were photobleached 2-4 days after transfection, and the recovery of fluorescence intensity tracked within the bleached and unbleached ROIs by laser scanning confocal microscopy. Granules formed by WT MATR3(dRRM1/2)-EGFP displayed internal rearrangement over the course of minutes consistent with liquid-like properties, as did all tested disease mutants on the dRRM1/2 background (Fig. 5C-D). The S85C mutation, however, severely slowed fluorescence recovery, suggesting reduced exchange of molecules within each droplet. Using the Stokes-Einstein equation, we calculated viscosity estimates for each MATR3(dRRM1/2)-EGFP variant based on return time and bleached area size (Fig. 5E). Consistent with the observed effect of this mutation on fluorescence recovery, the S85C mutation led to a pronounced increase in viscosity over that of WT and other disease-associated mutants.

We wondered whether this phenotype was specific to nuclear droplets formed by MATR3(dRRM1/2)-EGFP, or if full-length MATR3 carrying pathogenic mutations would also display reduced mobility. For this, we transfected primary neurons with full-length versions of MATR3(WT)-EGFP or disease-associated MATR3-EGFP variants and then

bleached a circular area in the center of the nucleus (Fig. 5F). In each case, we noted rapid return of fluorescence, and the recovery rate was unaffected by pathogenic *MATR3* point mutations (Fig. 5G). To account for the rapidity of return as well as the area of the bleached region, we calculated a diffusion coefficient (DC) for each construct. Comparison of the DCs for WT and mutant MATR3-EGFP variants showed no significant differences (Fig. 5H). Our data therefore suggest that the S85C point mutation—and perhaps other mutations that cluster in the N-terminal disordered domain—selectively affect the droplet properties of MATR3.

Mapping the sequence determinants of MATR3 localization in neurons

Cytoplasmic inclusions composed of the RBP TDP-43 are characteristic of ALS and the majority of FTD (Arai et al., 2006; Neumann et al., 2006). Moreover, pathogenic mutations in the gene encoding TDP-43 enhance cytoplasmic mislocalization concordant with enhanced neurotoxicity, and reductions in cytoplasmic TDP-43 prolong neuronal survival (Barmada et al., 2010; Barmada et al., 2014). To determine if MATR3 localization is likewise an important determinant of neurodegeneration, we sought to disrupt the MATR3 nuclear localization signal (NLS). However, since multiple sequences have been associated with nuclear MATR3 localization (Hibino et al., 2006; Hisada-Ishii et al., 2007), we systematically identified regions enriched in positively-charged amino acids (arginine, lysine) that may mediate nuclear import via importin-α. We then deleted each of the 7 regions defined in this manner, including two that had been identified as controlling nuclear localization in previous studies, and assessed their localization by transfection in rodent primary cortical neurons followed by fluorescence microscopy (Fig. 6A).

Deletion of NLSs 1, 2, 3, 5, 6, and 7 had little to no effect on neuronal MATR3 distribution (Fig. 6B). While the dNLS3 mutation did not change nuclear MATR3 localization *per se*, it did induce the formation of many small, nuclear granules. This effect is consistent with the position of NLS3 within RRM2, and the observed formation of nuclear puncta upon RRM2 deletion (Fig. 4). In contrast, and in accord with previous studies (Hisada-Ishii et al., 2007), deletion of the bipartite NLS4 elicited a marked reduction in nuclear MATR3-EGFP accompanied by enhanced cytoplasmic localization and the formation of small MATR3-EGFP granules within the cytoplasm. In DT40 and HeLa cells, both NLS4 arms were critical for MATR3 nuclear localization (Hisada-Ishii et al., 2007). To determine if this is the case in neurons, we sequentially deleted the N- and C-terminal arms (dNLS4N and dNLS4C, respectively) and tested their localization by transfection into primary cortical neurons. These studies demonstrated that the N-terminal arm is necessary and sufficient for nuclear localization, as MATR3(dNLS4N)-EGFP exhibits nuclear clearing and punctate distribution in the cytoplasm and neuronal processes, while MATR3(dNLS4C)-EGFP has the same distribution as MATR3(WT)-EGFP (Fig. 6C-D).

Having identified the N-terminal arm of NLS4 as the key sequence regulating MATR3 localization in neurons, we asked whether driving MATR3 into the cytoplasm by deletion of this sequence could modify toxicity. Rodent primary cortical neurons were transfected with mApple and either EGFP, MATR3(WT)-EGFP, or MATR3(dNLS4N)-EGFP and imaged at regular intervals by LFM. Automated survival analysis of neuronal populations expressing these constructs demonstrated that the dNLS4N mutation and resulting cytoplasmic localization significantly reduced MATR3-dependent toxicity compared to the MATR3(WT)-EGFP (Fig. 6E). Therefore, unlike TDP-43 and FUS, two RBPs whose cytoplasmic mislocalization are tightly tied to neurodegeneration in ALS/FTD models, cytoplasmic MATR3 retention mitigates toxicity, suggesting that

nuclear MATR3 functions are required for neurodegeneration (Barmada et al., 2010; Qiu et al., 2014).

Given the observed relationship between MATR3 localization and toxicity, we wondered if subtle changes in nucleocytoplasmic MATR3 distribution could be responsible for the increased toxicity of MATR3 bearing disease-associated mutations. Rodent primary cortical neurons transfected with each of the pathogenic MATR3-EGFP variants showed no obvious difference in subcellular localization in comparison with MATR3(WT)-EGFP (Fig. 2A). To investigate MATR3-EGFP localization in a quantitative manner, we developed a customized image-based analysis script to draw ROIs around the nucleus and soma of each neuron, measure MATR3-EGFP content separately within each compartment, and calculate a nucleocytoplasmic ratio for MATR3-EGFP in individual cells (Fig. 6F). This analysis confirmed our initial observations, showing no significant differences in the localization of mutant MATR3-EGFP variants compared to MATR3(WT)-EGFP.

In a complementary series of experiments, we utilized biochemical fractionation to assess the distribution of MATR3-EGFP in a human cell line. MATR3(WT)-EGFP or versions of MATR3-EGFP bearing the S85C, F115C, P154S, and T622A disease-associated mutations were transfected into HEK293T cells, and the nuclear and cytoplasmic fractions subjected to SDS-PAGE and Western blotting. In agreement with single-cell data from transfected primary neurons, we noted no difference in the nucleocytoplasmic distribution of any of the MATR3-EGFP variants tested here (Fig. 6G). Nevertheless, we consistently observed far less of the S85C variant in both nuclear and cytoplasmic fractions, compared to MATR3(WT)-EGFP and other disease-associated mutants. These data suggest that the S85C mutation may destabilize MATR3-EGFP; alternatively, this mutation may prevent adequate solubilization and detection of MATR3-EGFP via SDS-PAGE and Western blotting.

A subset of pathogenic MATR3 mutations affect protein solubility but not stability

To discriminate among these possibilities, we first investigated the turnover of WT and mutant MATR3 variants using optical pulse labeling (OPL), a technique enabling non-invasive determinations of protein clearance in living cells (Barmada et al., 2014). For these experiments, MATR3 was fused to Dendra2—a photoconvertable protein that irreversibly switches from a green to red fluorescent state upon illumination with low-wavelength light (Chudakov et al., 2007)—and expressed in primary cortical neurons. One day after transfection, neurons were illuminated with blue light to photoconvert Dendra2, and the time-dependent loss of red fluorescence signal used to calculate protein half-life (Fig. 7A). Previous studies validated the accuracy and utility of OPL for determinations of protein half-life (Barmada et al., 2014); importantly, and in contrast to biochemical techniques for calculating half-life that depend on radioactive labeling or translational inhibitors, OPL allows us to measure protein clearance on a single-cell level for thousands of neurons simultaneously (Fig. 7B). Most disease-associated mutations had little effect upon the turnover of MATR3-Dendra2 in primary cortical neurons. However, we noted subtle destabilization of MATR3(S85C)-Dendra2 in comparison to other pathogenic mutant variants and MATR3(WT)-Dendra2 (Fig. 7C-D). Even so, the magnitude of the effect was relatively small, making it unlikely that differences in protein turnover fully explain the reduced abundance of MATR3(S85C)-EGFP noted in cell lysates (Fig. 6G).

We next asked if the S85C mutation altered MATR3 solubility. HEK293T cells transfected with WT and mutant MATR3-EGFP variants were lysed using a harsher protocol that involved sonication in RIPA buffer; additionally, we used urea buffer to extract all RIPA-insoluble proteins. In stark contrast to mild conditions (Fig. 6G), harsher

lysis resulted in equivalent levels of all MATR3 variants on Western blot, suggesting that the S85C mutation reduced MATR3 solubility (Fig. 7E). Consistent with this interpretation, the urea-soluble fraction was markedly enriched for MATR3(S85C)-EGFP and modestly enriched for MATR3(T622A)-EGFP. These data show that the S85C and T622A mutations reduce the solubility of MATR3, without drastically affecting its stability. As shown in Fig. 1A, both mutations lie within areas of predicted disorder, consistent with their effects on MATR3 aggregation and solubility.

DISCUSSION

In this study, we modeled MATR3-mediated neurodegeneration by overexpressing WT or disease-associated MATR3 variants in primary neurons. In doing so, we found that neurons were highly susceptible to increases or decreases in MATR3 levels, and disease-associated MATR3 variants exhibited enhanced toxicity in comparison to MATR3(WT). Structure-function studies demonstrated that the ZF2 domain modulates overexpression-related toxicity, while RRM2 prevents MATR3 phase separation into mobile nuclear puncta. Biophysical analysis of these puncta confirmed their liquid-like nature and further indicated that the pathogenic S85C mutation substantially increased the viscosity of these structures. We also determined that the N-terminal arm of a bipartite NLS drives MATR3 nuclear localization; forcing MATR3 into the cytoplasm by deleting this sequence blocked toxicity from MATR3 overexpression. While we did not observe any differences in the distribution of pathogenic MATR3 variants, we noted that the S85C mutation significantly reduced MATR3 solubility and, to a lesser extent, stability. The T622A mutant displayed similar but more muted effects on MATR3 solubility, suggesting that disease-associated mutations located in distinct MATR3 domains may operate through convergent pathogenic mechanisms.

Both MATR3 overexpression and knockdown elicited significant and comparable toxicity in neurons. These data suggest that neurons are bidirectionally vulnerable to changes in MATR3 levels. Post-mortem studies of MATR3 distribution in sporadic and familial ALS patients demonstrated stronger MATR3 nuclear staining as well as the presence of cytoplasmic MATR3 aggregates in motor neurons (Dreser et al., 2017; Tada et al., 2017). While the impact of these findings is unknown, MATR3 mislocalization or sequestration into aggregates may reflect a reduction in normal function, a new and abnormal function, or both. In mice, homozygous *Matr3* knockout is embryonic lethal, while heterozygous *Matr3*$^{+/-}$ animals demonstrate incompletely penetrant cardiac developmental abnormalities. However, *Matr3*$^{+/-}$ mice exhibited roughly equivalent Matr3 protein levels in comparison to nontransgenic animals, complicating any conclusions regarding Matr3 loss-of-function in these models (Quintero-Rivera et al., 2015). Overexpression of human MATR3(F115C) in mice results in severe muscle disease consisting of fore- and hindlimb muscle atrophy accompanied by vacuolization (Moloney et al., 2016). These animals also displayed spinal cord gliosis and cytoplasmic MATR3 redistribution in spinal motor neurons akin to changes in MATR3 localization noted in humans with ALS, although no significant neurodegeneration was observed in MATR3(F115C) transgenic mice. Our data illustrating the dose-dependency of MATR3 neurotoxicity (Fig. 1) imply that MATR3(F115C) expression may be insufficient to elicit neurodegeneration in these animals. Alternatively, constitutive overexpression of MATR3(F115C) in transgenic mice may trigger compensatory mechanisms during development that promote neuronal survival.

MATR3 is unique among ALS/FTD-associated RBPs in possessing not just two tandem RRMs but also two ZF domains that can bind repetitive DNA elements found in the nuclear scaffold, consistent with MATR3's localization within the nuclear matrix (Hibino et al., 1998). We attempted to identify which functional domains were important

for MATR3 overexpression toxicity and found that while deletion of ZF2 resulted in modest rescue, deletion of RRM2—either alone or in combination with RRM1—resulted in the formation of phase-separated intranuclear droplets. Our data therefore support a model in which RNA binding prevents MATR3 self-association into droplets. Consistent with this interpretation, we observed small, mobile MATR3 granules in the cytoplasm and neuronal processes when the bipartite NLS was disrupted (Fig. 6D). Cytoplasmic RNA concentrations are more than an order of magnitude lower than those in the nucleus, a gradient that may favor the coalescence of MATR3(dNLS4N)-EGFP into puncta within the neuronal soma and processes (Goldstein and Trescott, 1970).

The functional importance of the individual RRM domains for MATR3's RNA binding activity is unclear; while some studies suggest that both RRM1 and RRM2 bind RNA, other investigations indicated that RRM2 is primarily responsible for binding RNA (Hibino et al., 2006; Salton et al., 2011). Our data show that deletion of RRM2 is sufficient to elicit phase separation by MATR3, suggesting that RNA recognition by MATR3 is mediated largely by RRM2. We also noted no significant difference in the survival of neuronal populations overexpressing dRRM1, dRRM2, and dRRM1/2 variants of MATR3-EGFP, implying that RNA binding *per se* is unrelated to MATR3-mediated neurodegeneration. This interpretation is strengthened by detailed analyses of neurons expressing MATR3(dRRM2) and MATR3(dRRM1/2). When neurons with and without droplets were assessed separately, we noted that neurons exhibiting diffuse MATR3(dRRM2) or MATR3(dRRM1/2) displayed a significantly higher risk of death than those with droplets. These results imply that diffuse MATR3, when not bound to RNA, can be highly toxic. Conversely, sequestration of RNA-binding deficient MATR3 into puncta is associated with extended neuronal survival. Our data further indicate that diffuse MATR3(dRRM1/2) is more toxic than diffuse MATR3(dRRM2) (compare the diffuse population in Fig. 4G to the diffuse population in Fig. 4H). Since RRM1 may be

476 capable of recognizing some RNA even without RRM2, these observations suggest that
477 neurodegeneration is inversely proportional to the ability of MATR3 to bind RNA when
478 diffusely localized within the nucleus. In disease models involving related RBPs,
479 including TDP-43 and FUS, toxicity requires the presence of RNA binding motifs as well
480 as low-complexity domains that enable LLPS (Johnson et al., 2008; Daigle et al., 2013;
481 Ihara et al., 2013). As with MATR3, abrogation of RNA binding may disinhibit self-
482 association, resulting in the sequestration of otherwise toxic diffuse protein within
483 droplets.

484 Investigating the liquid-like properties of MATR3(dRRM1/2)-EGFP droplets, we
485 noted a selective effect of the S85C mutation on droplet viscosity. Low-complexity,
486 intrinsically disordered domains are required for phase separation and self-assembly of
487 RBPs. Apart from its nucleic acid binding domains, MATR3 displays a high degree of
488 predicted disorder based on its primary amino acid sequence (Fig. 1A). The location of
489 the S85C mutation and its effects on MATR3(dRRM2)-EGFP droplet viscosity suggest
490 that the N-terminal disordered region of MATR3 regulates the liquid-like properties of
491 droplets. Whether full-length MATR3 is capable of phase-separation under physiological
492 circumstances, and what relevance this process has for disease, is currently unclear.

493 Conflicting evidence (Hibino et al., 2006; Hisada-Ishii et al., 2007) suggests that
494 MATR3 nuclear import is driven by distinct sequences in different cell types. For
495 example, while amino acids 701-718 are essential for nuclear localization of rat MATR3
496 in Ac2F cells, deletion of the homologous sequence (amino acids 701-720) in human
497 MATR3 has no effect on neuronal distribution (Fig. 6B). To identify the sequences
498 responsible for MATR3 nuclear import within neurons, we undertook a systematic
499 analysis of arginine/lysine-rich sequences in MATR3 resembling NLSs. In accord with an
500 earlier report (Hisada-Ishii et al., 2017), we found that MATR3's bipartite NLS (NLS4)
501 controlled its nuclear enrichment in neurons, but only the N-terminal arm of the NLS was

sufficient for MATR3 nuclear clearing and cytoplasmic distribution. Pathogenic *TARDBP* and *FUS* mutations promote cytoplasmic mislocalization of TDP-43 and FUS, respectively, and cytoplasmic enrichment of these proteins is tightly linked to toxicity (Barmada et al., 2010; Dormann et al., 2010). In stark contrast, however, we observed that cytoplasmic MATR3 redistribution extended neuronal survival, suggesting—along with the partial rescue we observed for MATR3(dZF2)-EGFP and MATR3(dZF1/2)-EGFP—that MATR3 overexpression elicits neurodegeneration through nuclear DNA binding activity, mediated at least in part by ZF2.

Given previously established relationships between the distribution and aggregation of RBPs and neurodegeneration in ALS models (Johnson et al., 2009; Barmada et al., 2010; Dormann et al., 2010; Igaz et al., 2011; Kim et al., 2013; Qiu et al., 2014), we wondered whether the enhanced toxicity of pathogenic MATR3 variants arises from mutation-associated changes in MATR3 localization or solubility. We noted no significant differences in the subcellular distribution of mutant MATR3 variants in comparison to MATR3(WT), but instead consistently observed reduced levels of MATR3(S85C) in transfected cell lysates. A similar pattern was noted in previous investigations and attributed to reduced MATR3(S85C) stability (Johnson et al., 2014). Using OPL, a sensitive method for measuring protein turnover *in situ* (Barmada et al., 2014; Gupta et al., 2017), we detected only a very modest shortening of MATR3(S85C) half-life compared to MATR3(WT). Nevertheless, we observed a marked change in the solubility of MATR3(S85C) and, less so, MATR3(T622A). This is in partial agreement with initial studies of MATR3(S85C) that noted equivalent amounts of MATR3(WT) and MATR3(S85C) in insoluble fractions but reduced MATR3(S85C) in the nuclear fraction (Senderek et al., 2009). Both the S85C and T622A mutations lie within domains predicted to be disordered (Fig. 1). Furthermore, both mutations disrupt potential phosphorylation sites, and phosphorylation within the intrinsically disordered domain of

FUS inhibits self-association of the protein through negative-negative charge repulsion between phosphate groups (Monahan et al., 2017). Of the 13 pathogenic mutations identified to date in MATR3, four (S85C, S610F, T622A, S707L) eliminate phosphorylatable residues, suggesting that inadequate phosphorylation and subsequent disinhibited self-association of MATR3 may be a conserved feature of MATR3 mutants.

MATR3's possesses broad functions in DNA/RNA processing (Belgrader et al., 1991; Hibino et al., 2000; Zhang and Carmichael, 2001; Salton et al., 2014; Coelho et al., 2015; Rajgor et al., 2016; Uemura et al., 2017). Its presence within cytoplasmic aggregates in approximately half of patients with sporadic ALS (Tada et al., 2017) implies that MATR3 pathology causes or is caused by cellular alterations in RNA and protein homeostasis, many of which may contribute to neurodegeneration in ALS and related disorders. Our work confirms that MATR3 is essential for maintaining neuronal survival and furthermore shows that MATR3 accumulation results in neurodegeneration in a manner that depends on its subcellular localization and ZF domains. Additional studies are required to further delineate the impact of disease-associated MATR3 mutations on the function, behavior, and liquid-like properties of MATR3.

MATERIALS AND METHODS

Plasmids

Full-length human *MATR3* cDNA was obtained from Addgene (#32880) and cloned into the pCMV-Tag2B vector (Agilent Technologies, #211172, Santa Clara, CA) using BamHI and XhoI endonucleases, tagging the amino-terminus with a FLAG epitope. To generate MATR3-EGFP, the *EGFP* open reading frame with a 14 amino acid N-terminal linker was amplified from pGW1-EGFP (Arrasate et al., 2004) by PCR using forward primer AGC TAC TAG TAC TAG AGC TGT TTG GGA C and reverse primer TAT TGG GCC CCT ATT ACT TGT ACA GCT CGT CCA T. The resulting amplicon was

554 digested with SpeI and ApaI and cloned into the corresponding sites in pKS to generate
555 pKS-EGFP. To create pKS-MATR3-EGFP, the *FLAG-MATR3* open reading frame from
556 pCMV-Tag2B was amplified by PCR with forward primer GAT CTC TAG AGC GGC
557 CGC CAC CAT GGA T and reverse primer AGC TAC TAG TCA TAG TTT CCT TCT
558 TCT GTC T, digested with XbaI and SpeI, and inserted into the corresponding sites in
559 pKS-EGFP. pGW1-MATR3-EGFP was generated by digesting pKS-MATR3-EGFP with
560 XbaI and ApaI, purifying the ensuing fragment containing MATR3-EGFP, and inserting
561 into the corresponding sites of pGW1. To create Dendra2-tagged MATR3 variants, the
562 *EGFP* coding region of each construct was removed by PCR amplification of the pGW1-
563 MATR3-EGFP vector using primers that flank the *EGFP* open reading frame. The
564 *Dendra2* open reading frame was then removed from pGW1-Dendra2 (Barmada et al.,
565 2014) by digestion with ApaI and MfeI, and inserted into pGW1-MATR3. All constructs
566 were confirmed by sequencing prior to transfection in neurons and HEK293T cells.
567 Domain deletion mutants were created using Q5 Hot Start High-Fidelity DNA
568 Polymerase (New England Biolabs, Ipswich, MA) and primers flanking the regions to be
569 deleted for nucleic acid-binding domain (Table 1) and putative nuclear localization signal
570 (Table 2) deletions. All disease-associated point mutations were created with site-
571 directed mutagenesis (Table 3).
572
573 *Primary neuron cell culture and transfection*
574 Cortices from embryonic day (E)19-20 Long-Evans rat embryos were dissected
575 and disassociated, and primary neurons plated at a density of 6 x 10^5 cells/mL in 96-well
576 plates, as described previously (Saudou et al., 1998). At *in vitro* day (DIV) 4-5, neurons
577 were transfected with 100 ng of pGW1-mApple (Barmada et al., 2014) to mark cells
578 bodies and 100 ng of an experimental construct (i.e. pGW1-MATR3-EGFP) using
579 Lipofectamine 2000, as before (Barmada et al., 2010). Following transfection, cells were

placed into either Neurobasal with B27 supplement (Gibco, Waltham, MA; for all survival experiments) or NEUMO photostable medium (Cell Guidance Systems, Cambridge, UK; for optical pulse labeling experiments). For siRNA knockdown experiments, neurons were transfected with 100 ng of pGW1-mApple per well and siRNA at a final concentration of 90 nM. Cells were treated with either scrambled siRNA (Dharmacon, Lafayette, CO) or siRNA targeting the N-terminal coding region of rat Matr3 (5' GUC AUU CCA GCA GUC AUC UUU 3').

Longitudinal fluorescence microscopy and automated image analysis

Neurons were imaged as described previously (Barmada et al., 2015) using a Nikon (Tokyo, Japan) Eclipse Ti inverted microscope with PerfectFocus3 and a 20X objective lens. Detection was accomplished with an Andor (Belfast, UK) iXon3 897 EMCCD camera or Andor Zyla4.2 (+) sCMOS camera. A Lambda XL Xenon lamp (Sutter) with 5 mm liquid light guide (Sutter Instrument, Novato, CA) was used to illuminate samples, and custom scripts written in Beanshell for use in μManager controlled all stage movements, shutters, and filters. Custom ImageJ/Fiji macros and Python scripts were used to identify neurons and draw regions of interest (ROIs) based upon size, morphology, and fluorescence intensity. Criteria for marking cell death involved rounding of the soma, loss of fluorescence and degeneration of neuritic processes. Custom scripts were also used to identify and draw bounding ROIs around nuclei of transfected cells based upon MATR3-EGFP or Hoechst 33258 (ThermoFisher, Waltham, MA) fluorescence. Coefficient of variation (CV) was calculated as the standard deviation of fluorescence intensity divided by the mean fluorescence intensity within an ROI.

Immunocytochemistry

Neurons were fixed with 4% paraformaldehyde, rinsed with phosphate buffered saline (PBS), and permeabilized with 0.1% Triton X-100 in PBS. After brief treatment with 10 mM glycine in PBS, cells were placed in blocking solution (0.1% Triton X-100, 2% fetal calf serum, and 3% bovine serum albumin (BSA), all in PBS) at room temperature (RT) for 1 h before incubation in primary antibody, rabbit anti-MATR3 (Abcam EPR10634(B), Cambridge, UK) diluted 1:1000 in blocking solution, overnight at 4 °C. Cells were then washed 3x in PBS and incubated at RT with secondary antibody, goat anti-rabbit 647 (ThermoFisher A-21245) diluted 1:1000 in blocking solution, for 1 h at RT. Following 3x rinses in PBS containing 1:5000 Hoechst 33258 dye (ThermoFisher), neurons were imaged by fluorescence microscopy, as described above.

Fluorescence recovery after photobleaching

Primary neurons were dissected as above and plated in 8-well borosilicate chambers (LAB-TEK). On DIV 3, they were transfected as before but using 200 µg of pGW1-mApple and 200 µg of pGW1-MATR3-EGFP variants per well. Cell were imaged 2-4 days after transfection using a Nikon A1 confocal microscope operated by Nikon Elements, a 60X objective lens, and a heating chamber with CO_2 pre-warmed to 37 °C. For MATR3(dRRM1/2)-EGFP variants, an ROI corresponding to half of the granule was outlined with Elements and photobleached using a 488 nm laser set at 30% power, 1 pulse per sec x 7 sec. Fluorescence recovery was monitored up to 10 min after photobleaching. For full-length MATR3 variants, ROIs for photobleaching were drawn in the center of the nucleus for each cell, and recovery was monitored for 6 min.

Image analysis was conducted in FIJI. Rigid body stack registration was used to fix the granules in place relative to the frame. The GFP integrated density for the whole granule was calculated from pre-bleach measurements, as was the fraction of granule

631 integrated density corresponding to the ROI to be photobleached. The decline in this
632 fraction immediately after photobleaching was then calculated and used as the floor, and
633 the return was plotted as the percent recovery within the ROI as a fraction of the original
634 pre-bleach granule integrated density.

635 Recovery data were fit to the equation $y(t) = A(1-e^{-\tau t})$, where A is the return curve
636 plateau, τ is the time constant, and t is the time post-bleach. The fitted τ from each curve
637 was then used to calculate the time to half-return ($t_{1/2}$) using the equation $t_{1/2} = \ln(0.5)/-\tau$.
638 To estimate the diffusion coefficient (D) of these molecules, we used the equation $D =$
639 $(0.88w^2)/(4t_{1/2})$, where w is the ROI radius (Gopal et al., 2017). This equation assumes
640 spot bleach with a circular stimulation ROI and diffusion limited to the x-y plane. Since
641 we could not be confident that these assumptions were met, we estimated D and
642 downstream parameters by dividing ROI areas by π to approximate w^2 and solving for D.
643 This estimated value was used in the Einstein-Stokes equation, $D = k_BT/(6\pi\eta r)$, where k_B
644 is the Boltzmann constant, T is temperature in K, η is viscosity, and r is the Stokes
645 radius of the particle. As there is no applicable structural data on MATR3, we estimated
646 a Stokes radius of 3.13 nm by applying the MATR3(dRRM1/2)-EGFP fusion protein's
647 combined molecular weight of 106.4 kDa to the equation $R_{min} = 0.66M^{1/3}$, where R_{min} is
648 the minimal radius in nm of a sphere that could bound a globular protein with a
649 molecular weight of M (Erickson, 2009). Using these constants and the estimated D for
650 each granule, the Einstein-Stokes equation was rearranged to solve for η.

651 Photobleaching data from full-length MATR3-EGFP was analyzed in a similar
652 fashion. After calculating the nuclear integrated density, the fraction attributable to
653 photobleaching within the ROI was used for normalization. Intensity data were fit to the
654 $y(t) = A(1-e^{-\tau t})$ equation, $t_{1/2}$ values were calculated as before, and D determined by the
655 equation $D = (0.88w^2)/(4t_{1/2})$.
656

Nuclear/cytoplasmic fractionation and differential solubility

HEK293T cells were transfected in a 6-well plate with 3 µg of DNA per well using Lipofectamine 2000 according to the manufacturer's instructions. For nuclear/cytoplasmic fractionation, cells were washed with cold PBS 24 h after transfection, collected with resuspension buffer (10 mM Tris, 10 mM NaCl, 3 mM $MgCl_2$, pH 7.4), and transferred to a pre-chilled 1.5 mL conical tube to sit on ice for 5 min. An equal volume of resuspension buffer with 0.6% Igepal (Sigma, St. Louis, MO) was then added to rupture cell membranes and release cytoplasmic contents, with occasional inversion for 5 min on ice. Nuclei were pelleted at 100 x g at 4 °C for 10 min using a tabletop centrifuge. The supernatant (cytosolic fraction) was collected, and the nuclei were rinsed twice in resuspension buffer without Igepal. To collect nuclear fractions, pelleted nuclei were lysed in RIPA buffer (Pierce) with protease inhibitors (Roche, Mannheim, Germany) on ice for 30 min with occasional inversion. Samples were centrifuged at 9,400 x g at 4 °C for 10 min, and the supernatant was saved as the nuclear fraction.

For differential solubility experiments, transfected HEK293T were collected in cold PBS 24 h after transfection and transferred to a pre-chilled conical tube on ice. Cells were then centrifuged at 100 x g for 5 min at 4 °C to pellet cells, the PBS was aspirated, and cells were resuspended in RIPA buffer with protease inhibitors. Following lysis on ice for 15 min with occasional inversion, cells were sonicated at 80% amplitude with 5 sec on/5 sec off for 2 min using a Fisherbrand Model 505 Sonic Dismembrenator (ThermoFisher). Samples were centrifuged at 41,415 x g for 15 min at 4 °C to pellet RIPA-insoluble material, with the supernatant removed and saved as the RIPA-soluble fraction. The RIPA-insoluble pellet was washed in RIPA once, and contents resuspended vigorously in urea buffer (7 M urea, 2 M thiourea, 4% CHAPS, 30 mM Tris,

682 pH 8.5). Samples were again centrifuged at 41,415 x g for 15 min at 4 °C, and the
683 supernatant was saved as the RIPA-insoluble, urea-soluble fraction.
684 For SDS-PAGE, stock sample buffer (10% SDS, 20% glycerol, 0.0025%
685 bromophenol blue, 100 mM EDTA, 1 M DTT, 20 mM Tris, pH 8) was diluted 1:10 in
686 lysates and all samples except urea fractions were boiled for 10 min before 5-15 µg of
687 protein were loaded onto 4-15% gradient gels (Bio-Rad, Hercules, CA). For urea
688 fractions, total protein concentration was too low to quantify and so equal volumes of
689 sample across conditions were mixed 1:1 with water and loaded. After electrophoresis,
690 samples were transferred at 30 V overnight at 4 °C onto an activated 2 µm nitrocellulose
691 membrane (Bio-Rad), blocked with 3% BSA in 0.2% Tween-20 in Tris-buffered saline
692 (TBST), and blotted overnight at 4 °C with the following primary antibodies: rabbit anti-
693 MATR3 (Abcam EPR10634(B)), mouse anti-GAPDH (Millipore Sigma MAB374), and
694 rabbit anti-H2B (Novus NB100-56347), all diluted 1:1000 in 3% BSA, 0.2% TBST. The
695 following day, blots were washed in 0.2% TBST, incubated at RT for 1 h with AlexaFluor
696 goat anti-mouse 594 (ThermoFisher A-11005) and goat anti-rabbit 488 (ThermoFisher
697 A-11008), both diluted 1:10,000 in 3% BSA in 0.2% TBST. Following treatment with
698 secondary antibody, blots were washed in 0.2% TBST, placed in Tris-buffered saline,
699 and imaged using an Odyssey CLx Imaging System (LI-COR, Lincoln, NE).
700
701 *Statistical analysis*
702 Statistical analyses were performed in R or Prism 7 (GraphPad). For primary
703 neuron survival analysis, the publically available R survival package was used to
704 determine hazard ratios describing the relative survival among populations through Cox
705 proportional hazards analysis. For half-life calculations, a custom R script was applied to
706 fit log-transformed TRITC intensity data to a linear equation. Photobleaching recovery
707 data were fit to the $y(t) = A(1-e^{-\tau t})$ equation using non-linear regression in R. siRNA

knockdown data were plotted using Prism 7, and significance determined via the two-tailed t-test. One-way ANOVA with Tukey's post-test was used to assess for significant differences among nuclear/cytoplasmic ratios, viscosities, D values, and half-lives. Data are shown as mean ± SEM unless otherwise stated.

Table 1

Deletion mutation	Amino acids	Primers	Sequences
dZF1	288 –322	Forward	CTT GAA ATC TAC CCA GAA TG
		Reverse	CTT CGG TAA GAG TCC ATG
dZF2	798 – 833	Forward	CTG AAT AAA TTG GCA GAA GAA C
		Reverse	AGG TAT CAC ATA GTC TAT ACC
dRRM1	398 – 473	Forward	TAT AAA AGA ATA AAG AAA CCT GAA GG
		Reverse	GCT AGT TTC CAC TCT GCC
dRRM2	496 – 575	Forward	GTT CTG AGG ATT CCA AAC AG
		Reverse	TCC AAG CTC TTG CTT TTG

Table 2

Deletion mutation	Amino acids	Primers	Sequences
dNLS1	146 – 171	Forward	AGA GTA CCT AGG GAT GAT TG
		Reverse	AAG CTG TAG AAG GAT TTG G
dNLS2	473 – 479	Forward	CCT GAA GGA AAG CCA GAT C
		Reverse	CTG GGA TAA ATG AAC TCT CAC
dNLS3	571 – 574	Forward	CTG GTT CTG AGG ATT CCA ACC
		Reverse	CTC AGA CAG GTC AAC CTT C
dNLS4	588 – 611	Forward	ACT GAT GGT TCC CAG AAG
		Reverse	CAG TAA ATC AAT GCC TCT G
dNLS5	701– 720	Forward	GAG GAA CTT GAT CAA GAA AAC
		Reverse	CAC AGC TTT ATC TGA TGG TTC
dNLS6	780 – 784	Forward	CAG CCC AAT GTT CCT GTT G
		Reverse	ATA CTC ATC TGG GAT TGT ATA G
dNLS7	798 – 833	Forward	GAA ACT ATG ACT AGT ACT AGA G
		Reverse	CTG ATA ATG AGG AAG GCT G
dNLS4N	588 – 595	Forward	TCT TAC TCT CCA GAT GGC
		Reverse	CAG TAA ATC AAT GCC TCT G
dNLS4C	608 – 611	Forward	ACT GAT GGT TCC CAG AAG
		Reverse	ATC ACT TGG AGA TTC TTT GC

716 **Table 3**

Mutation	Primers	Sequences
S85C	Forward	AAT TTG CAG TGT ATA TTT AAC ATT GG
	Reverse	ATG GGA AGA AGT ACT AGC AGA
F115C	Forward	ATT TTG GCC AGC TGT GGT CTG TCT GCT
	Reverse	GTT ACT GGC CTG GTC TGC ATC
P154S	Forward	GAA GAA GGC TCT ACC TTG AGT TAT GG
	Reverse	AGT TCT CCT CCT TTT AAG CTG
T622A	Forward	GAG AGT TCA GCC GAA GGT AAA GAA C
	Reverse	AGT CTT CTG GGA ACC ATC AGT

717

718
719
720 **ACKNOWLEDGEMENTS**

721 We thank Dr. Stephen Lentz for his assistance with confocal microscopy, Drs.
722 Claudia Figueroa-Romero and Hilary Archbold for their experimental advice, and Brittany
723 Flores for technical assistance in assembling the manuscript.
724 The present work was supported in part by funding from the National Institutes of Health
725 (NIH) National Institute for Neurological Disorders and Stroke (NINDS) R01 NS097542
726 (S.J.B.), National Institute for Aging (NIA) P30 AG053760 (S.J.B.), and National Institute
727 of General Medical Sciences (NIGMS) T32 GM007863 (A.M.M.) and T32 NS076401
728 (A.M.M.); the Protein Folding Diseases Initiative at the University of Michigan (S.J.B.);
729 the Program for Neurology Research and Discovery (E.L.F.); and the A. Alfred Taubman
730 Medical Research Institute (S.J.B., E.L.F.). Confocal microscopy was performed at the
731 Microscopy & Image Analysis Core of the Michigan Diabetes Research Center funded
732 by NIH grant P60DK020572 from the National Institute of Diabetes and Digestive and
733 Kidney Diseases (NIDDK).

734

735 **COMPETING INTERESTS**

736 The authors declare no competing interests.

AUTHOR CONTRIBUTIONS

A.M.M., Y.S.H., E.L.F., and S.J.B. designed the study; R.A.M. wrote original code for data analysis; X.L. performed primary neuron isolations; Y.S.H. created all MATR3 constructs and identified NLS-like sequences within MATR3; A.M.M. and Y.S.H. conducted neuronal survival experiments; A.M.M. performed all confocal microscopy and data analysis, and assembled all figures; A.M.M. and S.J.B. wrote the manuscript; A.M.M., S.J.B., Y.S.H and E.L.F. edited and revised the manuscript.

REFERENCES

Arai T, Hasegawa M, Akiyama H, Ikeda K, Nonaka T, Mori H, Mann D, Tsuchiya K, Yoshida M, Hashizume Y, Oda T (2006) TDP-43 is a component of ubiquitin-positive tau-negative inclusions in frontotemporal lobar degeneration and amyotrophic lateral sclerosis. Biochemical and Biophysical Research Communications 351:602–611.

Arrasate M, Finkbeiner S (2005) Automated microscope system for determining factors that predict neuronal fate. Proc Natl Acad Sci USA 102:3840–3845.

Arrasate M, Mitra S, Schweitzer ES, Segal MR, Finkbeiner S (2004) Inclusion body formation reduces levels of mutant huntingtin and the risk of neuronal death. Nature 431:805–810.

Barmada SJ, Finkbeiner S (2010) Pathogenic TARDBP mutations in amyotrophic lateral sclerosis and frontotemporal dementia: disease-associated pathways. Rev Neurosci 21:251–272.

Barmada SJ, Ju S, Arjun A, Batarse A, Archbold HC, Peisach D, Li X, Zhang Y, Tank EMH, Qiu H, Huang EJ, Ringe D, Petsko GA, Finkbeiner S (2015) Amelioration of toxicity

763 in neuronal models of amyotrophic lateral sclerosis by hUPF1. Proc Natl Acad Sci
764 USA 112:7821–7826.
765 Barmada SJ, Serio A, Arjun A, Bilican B, Daub A, Ando DM, Tsvetkov A, Pleiss M, Li X,
766 Peisach D, Shaw C, Chandran S, Finkbeiner S (2014) Autophagy induction
767 enhances TDP43 turnover and survival in neuronal ALS models. Nature Chemical
768 Biology 10:677–685.
769 Barmada SJ, Skibinski G, Korb E, Rao EJ, Wu JY, Finkbeiner S (2010) Cytoplasmic
770 mislocalization of TDP-43 is toxic to neurons and enhanced by a mutation
771 associated with familial amyotrophic lateral sclerosis. J Neurosci 30:639–649.
772 Belgrader P, Dey R, Berezney R (1991) Molecular cloning of Matrin 3. A 125-kilodalton
773 protein of the nuclear matrix contains an extensive acidic domain. The Journal of
774 Biological Chemistry 266:9893–9899.
775 Boehringer A, Garcia-Mansfield K, Singh G, Bakkar N, Pirrotte P, Bowser R (2017) ALS
776 Associated Mutations in Matrin 3 Alter Protein-Protein Interactions and Impede
777 mRNA Nuclear Export. Scientific Reports:1–14.
778 Brayer KJ, Kulshreshtha S, Segal DJ (2008) The protein-binding potential of C2H2 zinc
779 finger domains. Cell Biochem Biophys 51:9–19.
780 Burdach J, O'Connell MR, Mackay JP, Crossley M (2012) Two-timing zinc finger
781 transcription factors liaising with RNA. Trends Biochem Sci 37:199–205.
782 Charcot J-M, Joffroy A (1869) Deux cas d'atrophie musculaire progressive avec lésions de
783 la substance grise et de faisceaux antérolatéraux de la moelle épinière. Arch
784 Physiol Norm Pathol. 2, 744–754.
785 Christensen E (1987) Multivariate survival analysis using Cox's regression model.
786 Hepatology 7:1346–1358.
787 Chudakov DM, Lukyanov S, Lukyanov KA (2007) Tracking intracellular protein movements
788 using photoswitchable fluorescent proteins PS-CFP2 and Dendra2. Nat Protoc

789 2:2024–2032.

790 Coelho MB, Attig J, Bellora N, Konig J, Hallegger M, Kayikci M, Eyras E, Ule J, Smith CW

791 (2015) Nuclear matrix protein Matrin3 regulates alternative splicing and forms

792 overlapping regulatory networks with PTB. The EMBO Journal 34:653–668.

793 Conicella AE, Zerze GH, Mittal J, Fawzi NL (2016) ALS Mutations Disrupt Phase

794 Separation Mediated by α-Helical Structure in the TDP-43 Low-Complexity C-

795 Terminal Domain. Structure 24:1537–1549.

796 Daigle JG, Lanson NA, Smith RB, Casci I, Maltare A, Monaghan J, Nichols CD,

797 Kryndushkin D, Shewmaker F, Pandey UB (2013) RNA-binding ability of FUS

798 regulates neurodegeneration, cytoplasmic mislocalization and incorporation into

799 stress granules associated with FUS carrying ALS-linked mutations. Human

800 Molecular Genetics 22:1193–1205.

801 Dormann D, Rodde R, Edbauer D, Bentmann E, Fischer I, Hruscha A, Than ME,

802 Mackenzie IRA, Capell A, Schmid B, Neumann M, Haass C (2010) ALS-associated

803 fused in sarcoma (FUS) mutations disrupt Transportin-mediated nuclear import. The

804 EMBO Journal 29:2841–2857.

805 Dreser A, Vollrath JT, Sechi A, Johann S, Roos A, Yamoah A, Katona I, Bohlega S,

806 Wiemuth D, Tian Y, Schmidt A, Vervoorts JOR, Dohmen M, Beyer C, Anink J,

807 Aronica E, Troost D, Weis J, Goswami A (2017) The ALS-linked E102Q mutation in

808 Sigma receptor-1 leads to ER stress-mediated defects in protein homeostasis and

809 dysregulation of RNA-binding proteins. :1–17.

810 Erickson HP (2009) Size and shape of protein molecules at the nanometer level

811 determined by sedimentation, gel filtration, and electron microscopy. Biol Proced

812 Online 11:32–51.

813 Feit H, Silbergleit A, Schneider LB, Gutierrez JA, Fitoussi R-P, Réyès C, Rouleau GA, Brais

814 B, Jackson CE, Beckmann JS, Seboun E (1998) Vocal Cord and Pharyngeal

Weakness with Autosomal Dominant Distal Myopathy: Clinical Description and Gene Localization to 5q31. The American Journal of Human Genetics 63:1732–1742.

Gallego-Iradi MC, Clare AM, Brown HH, Janus C, Lewis J, Borchelt DR (2015) Subcellular Localization of Matrin 3 Containing Mutations Associated with ALS and Distal Myopathy Pandey U, ed. PLoS ONE 10:e0142144–15.

Goldstein L, Trescott OH (1970) Characterization of RNAs that do and do not migrate between cytoplasm and nucleus. Proc Natl Acad Sci USA 67:1367–1374.

Gopal PP, Nirschl JJ, Klinman E, Holzbaur ELF (2017) Amyotrophic lateral sclerosis-linked mutations increase the viscosity of liquid-like TDP-43 RNP granules in neurons. Proc Natl Acad Sci USA 114:E2466–E2475.

Gupta R, Lan M, Mojsilovic-Petrovic J, Choi WH, Safren N, Barmada S, Lee MJ, Kalb R (2017) The Proline/Arginine Dipeptide from Hexanucleotide Repeat Expanded C9ORF72 Inhibits the Proteasome. eNeuro 4:ENEURO.0249–16.2017.

Hibino Y, Ohzeki H, Hirose N, Sugano N (1998) Involvement of phosphorylation in binding of nuclear scaffold proteins from rat liver to a highly repetitive DNA component. Biochimica et Biophysica Acta (BBA) - Gene Structure and Expression 1396:88–96.

Hibino Y, Ohzeki H, Sugano N, Hiraga K (2000) Transcription Modulation by a Rat Nuclear Scaffold Protein, P130, and a Rat Highly Repetitive DNA Component or Various Types of Animal and Plant Matrix or Scaffold Attachment Regions. Biochemical and Biophysical Research Communications 279:282–287.

Hibino Y, Usui T, Morita Y, Hirose N, Okazaki M, Sugano N, Hiraga K (2006) Molecular properties and intracellular localization of rat liver nuclear scaffold protein P130. Biochimica et Biophysica Acta (BBA) - Gene Structure and Expression 1759:195–207.

840 Hisada-Ishii S, Ebihara M, Kobayashi N, KITAGAWA Y (2007) Bipartite nuclear localization
841 signal of matrin 3 is essential for vertebrate cells. Biochemical and Biophysical
842 Research Communications 354:72–76.
843 Igaz LM, Kwong LK, Lee EB, Chen-Plotkin A, Swanson E, Unger T, Malunda J, Xu Y,
844 Winton MJ, Trojanowski JQ, Lee VM-Y (2011) Dysregulation of the ALS-associated
845 gene TDP-43 leads to neuronal death and degeneration in mice. J Clin Invest
846 121:726–738.
847 Ihara R, Matsukawa K, Nagata Y, Kunugi H, Tsuji S, Chihara T, Kuranaga E, Miura M,
848 Wakabayashi T, Hashimoto T, Iwatsubo T (2013) RNA binding mediates
849 neurotoxicity in the transgenic Drosophila model of TDP-43 proteinopathy. Human
850 Molecular Genetics 22:4474–4484.
851 Johnson BS, McCaffery JM, Lindquist S, Gitler AD (2008) A yeast TDP-43 proteinopathy
852 model: Exploring the molecular determinants of TDP-43 aggregation and cellular
853 toxicity. Proc Natl Acad Sci USA 105:6439–6444.
854 Johnson BS, Snead D, Lee JJ, McCaffery JM, Shorter J, Gitler AD (2009) TDP-43 is
855 intrinsically aggregation-prone, and amyotrophic lateral sclerosis-linked mutations
856 accelerate aggregation and increase toxicity. The Journal of Biological Chemistry
857 284:20329–20339.
858 Johnson JO et al. (2010) Exome sequencing reveals VCP mutations as a cause of familial
859 ALS. Neuron 68:857–864.
860 Johnson JO et al. (2014) Mutations in the Matrin 3 gene cause familial amyotrophic lateral
861 sclerosis. Nat Neurosci 17:664–666.
862 Kabashi E, Valdmanis PN, Dion P, Spiegelman D, McConkey BJ, Vande Velde C,
863 Bouchard J-P, Lacomblez L, Pochigaeva K, Salachas F, Pradat P-F, Camu W,
864 Meininger V, Dupré N, Rouleau GA (2008) TARDBP mutations in individuals with
865 sporadic and familial amyotrophic lateral sclerosis. Nat Genet 40:572–574.

866 Kim HJ et al. (2013) Mutations in prion-like domains in hnRNPA2B1 and hnRNPA1 cause
867 multisystem proteinopathy and ALS. Nature 495:467–473.
868 Kimonis VE, Fulchiero E, Vesa J, Watts G (2008) VCP disease associated with myopathy,
869 Paget disease of bone and frontotemporal dementia: review of a unique disorder.
870 Biochim Biophys Acta 1782:744–748.
871 Klar J, Sobol M, Melberg A, Mäbert K, Ameur A, Johansson ACV, Feuk L, Entesarian M,
872 Orlén H, Casar-Borota O, Dahl N (2013) Welander distal myopathy caused by an
873 ancient founder mutation in TIA1 associated with perturbed splicing. Hum Mutat
874 34:572–577.
875 Kwiatkowski TJ et al. (2009) Mutations in the FUS/TLS gene on chromosome 16 cause
876 familial amyotrophic lateral sclerosis. Science 323:1205–1208.
877 Leblond CS, Gan-Or Z, Spiegelman D, Laurent SB, Szuto A, Hodgkinson A, Dionne-
878 Laporte A, Provencher P, de Carvalho M, Orrù S, Brunet D, Bouchard J-P,
879 Awadalla P, Dupré N, Dion PA, Rouleau GA (2016) Replication study of MATR3 in
880 familial and sporadic amyotrophic lateral sclerosis. Neurobiology of Aging
881 37:209.e17–209.e21.
882 Lin Y, Protter DSW, Rosen MK, Parker R (2015) Formation and Maturation of Phase-
883 Separated Liquid Droplets by RNA-Binding Proteins. Mol Cell 60:208–219.
884 Mackenzie IR et al. (2017) TIA1 Mutations in Amyotrophic Lateral Sclerosis and
885 Frontotemporal Dementia Promote Phase Separation and Alter Stress Granule
886 Dynamics. Neuron 95:808–816.e809.
887 Marangi G, Lattante S, Doronzio PN, Conte A, Tasca G, Monforte M, Patanella AK, Bisogni
888 G, Meleo E, La Spada S, Zollino M, Sabatelli M (2017) Matrin 3 variants are
889 frequent in Italian ALS patients. Neurobiology of Aging 49:218.e1–218.e7.
890 Millecamps S, De Septenville A, Teyssou E, Daniau M, Camuzat A, Albert M, LeGuern E,
891 Galimberti D, Brice A, Marie Y, Le Ber I, FTD-ALS1 TFRNOFA (2014) Genetic

analysis of matrin 3 gene in French amyotrophic lateral sclerosis patients and frontotemporal lobar degeneration with amyotrophic lateral sclerosis patients. Neurobiology of Aging 35:2882.e13–2882.e15.

Miller J, Arrasate M, Shaby BA, Mitra S, Masliah E, Finkbeiner S (2010) Quantitative relationships between huntingtin levels, polyglutamine length, inclusion body formation, and neuronal death provide novel insight into huntington's disease molecular pathogenesis. J Neurosci 30:10541–10550.

Molliex A, Temirov J, Lee J, Coughlin M, Kanagaraj AP, Kim HJ, Mittag T, Taylor JP (2015) Phase separation by low complexity domains promotes stress granule assembly and drives pathological fibrillization. Cell 163:123–133.

Moloney C, Rayaprolu S, Howard J, Fromholt S, Brown H, Collins M, Cabrera M, Duffy C, Siemienski Z, Miller D, Swanson MS, Notterpek L, Borchelt DR, Lewis J (2016) Transgenic mice overexpressing the ALS- linked protein Matrin 3 develop a profound muscle phenotype. Acta Neuropathologica Communications:1–12.

Monahan Z, Ryan VH, Janke AM, Burke KA, Rhoads SN, Zerze GH, O'Meally R, Dignon GL, Conicella AE, Zheng W, Best RB, Cole RN, Mittal J, Shewmaker F, Fawzi NL (2017) Phosphorylation of the FUS low-complexity domain disrupts phase separation, aggregation, and toxicity. The EMBO Journal 36:2951–2967.

Murray DT, Kato M, Lin Y, Thurber KR, Hung I, McKnight SL, Tycko R (2017) Structure of FUS Protein Fibrils and Its Relevance to Self-Assembly and Phase Separation of Low- Complexity Domains. Cell 171:615–620.e616.

Neumann M, Sampathu DM, Kwong LK, Truax AC, Micsenyi MC, Chou TT, Bruce J, Schuck T, Grossman M, Clark CM, McCluskey LF, Miller BL, Masliah E, Mackenzie IR, Feldman H, Feiden W, Kretzschmar HA, Trojanowski JQ, Lee VM-Y (2006) Ubiquitinated TDP-43 in frontotemporal lobar degeneration and amyotrophic lateral sclerosis. Science 314:130–133.

Origone P, Verdiani S, Bandettini Di Poggio M, Zuccarino R, Vignolo M, Caponnetto C, Mandich P (2015) A novel Arg147Trp MATR3 missense mutation in a slowly progressive ALS Italian patient. Amyotrophic Lateral Sclerosis and Frontotemporal Degeneration 16:530–531.

Patel A et al. (2015) A Liquid-to-Solid Phase Transition of the ALS Protein FUS Accelerated by Disease Mutation. Cell 162:1066–1077.

Peng K, Radivojac P, Vucetic S, Dunker AK, Obradovic Z (2006) Length-dependent prediction of protein intrinsic disorder. BMC Bioinformatics 7:208.

Qiu H et al. (2014) ALS-associated mutation FUS-R521C causes DNA damage and RNA splicing defects. J Clin Invest 124:981–999.

Quintero-Rivera F et al. (2015) MATR3 disruption in human and mouse associated with bicuspid aortic valve, aortic coarctation and patent ductus arteriosus. Human Molecular Genetics 24:2375–2389.

Rajgor D, Hanley JG, Shanahan CM (2016) Identification of novel nesprin-1 binding partners and cytoplasmic matrin-3 in processing bodies. Mol Biol Cell 27:3894–3902.

Salton M, Elkon R, Borodina T, Davydov A, Yaspo M-L, Halperin E, Shiloh Y (2011) Matrin 3 Binds and Stabilizes mRNA Papavasiliou N, ed. PLoS ONE 6:e23882–e23887.

Salton M, Lerenthal Y, Wang S-Y, Chen DJ, Shiloh Y (2014) Involvement of Matrin 3 and SFPQ/NONO in the DNA damage response. Cell Cycle 9:1568–1576.

Saudou F, Finkbeiner S, Devys D, Greenberg ME (1998) Huntingtin acts in the nucleus to induce apoptosis but death does not correlate with the formation of intranuclear inclusions. Cell 95:55–66.

Senderek J et al. (2009) Autosomal-Dominant Distal Myopathy Associated with a Recurrent Missense Mutation in the Gene Encoding the Nuclear Matrix Protein, Matrin 3. The American Journal of Human Genetics 84:511–518.

944 Shin Y, Brangwynne CP (2017) Liquid phase condensation in cell physiology and disease.
945 Science 357:eaaf4382–13.
946 Tada M, Doi H, Koyano S, Kubota S, Fukai R, Hashiguchi S, Hayashi N, Kawamoto Y,
947 Kunii M, Tanaka K, Takahashi K, Ogawa Y, Iwata R, Yamanaka S, Takeuchi H,
948 Tanaka F (2017) Matrin 3 is a component of neuronal cytoplasmic inclusions of
949 motor neurons in sporadic amyotrophic lateral sclerosis. The American Journal of
950 Pathology:1–36.
951 Taylor JP, Brown RH, Cleveland DW (2016) Decoding ALS: from genes to mechanism.
952 Nature 539:197–206.
953 Ticozzi N, Vance C, Leclerc AL, Keagle P, Glass JD, McKenna-Yasek D, Sapp PC, Silani
954 V, Bosco DA, Shaw CE, Brown RH, Landers JE (2011) Mutational analysis reveals
955 the FUS homolog TAF15 as a candidate gene for familial amyotrophic lateral
956 sclerosis. Am J Med Genet B Neuropsychiatr Genet 156B:285–290.
957 Uemura Y, Oshima T, Yamamoto M, Reyes CJ, Costa Cruz PH, Shibuya T, Kawahara Y
958 (2017) Matrin3 binds directly to intronic pyrimidine-rich sequences and controls
959 alternative splicing. Genes Cells 22:785–798.
960 Vance C et al. (2009) Mutations in FUS, an RNA processing protein, cause familial
961 amyotrophic lateral sclerosis type 6. Science 323:1208–1211.
962 Xu L, Li J, Tang L, Zhang N, Fan D (2016) MATR3 mutation analysis in a Chinese cohort
963 with sporadic amyotrophic lateral sclerosis. Neurobiology of Aging 38:218.e3–
964 218.e4.
965 Zhang Z, Carmichael GG (2001) The Fate of dsRNA in the Nucleus: A p54nrb-Containing
966 Complex Mediates the Nuclear Retention of Promiscuously A-to-I Edited RNAs. Cell
967 106:465–476.

Figure 1

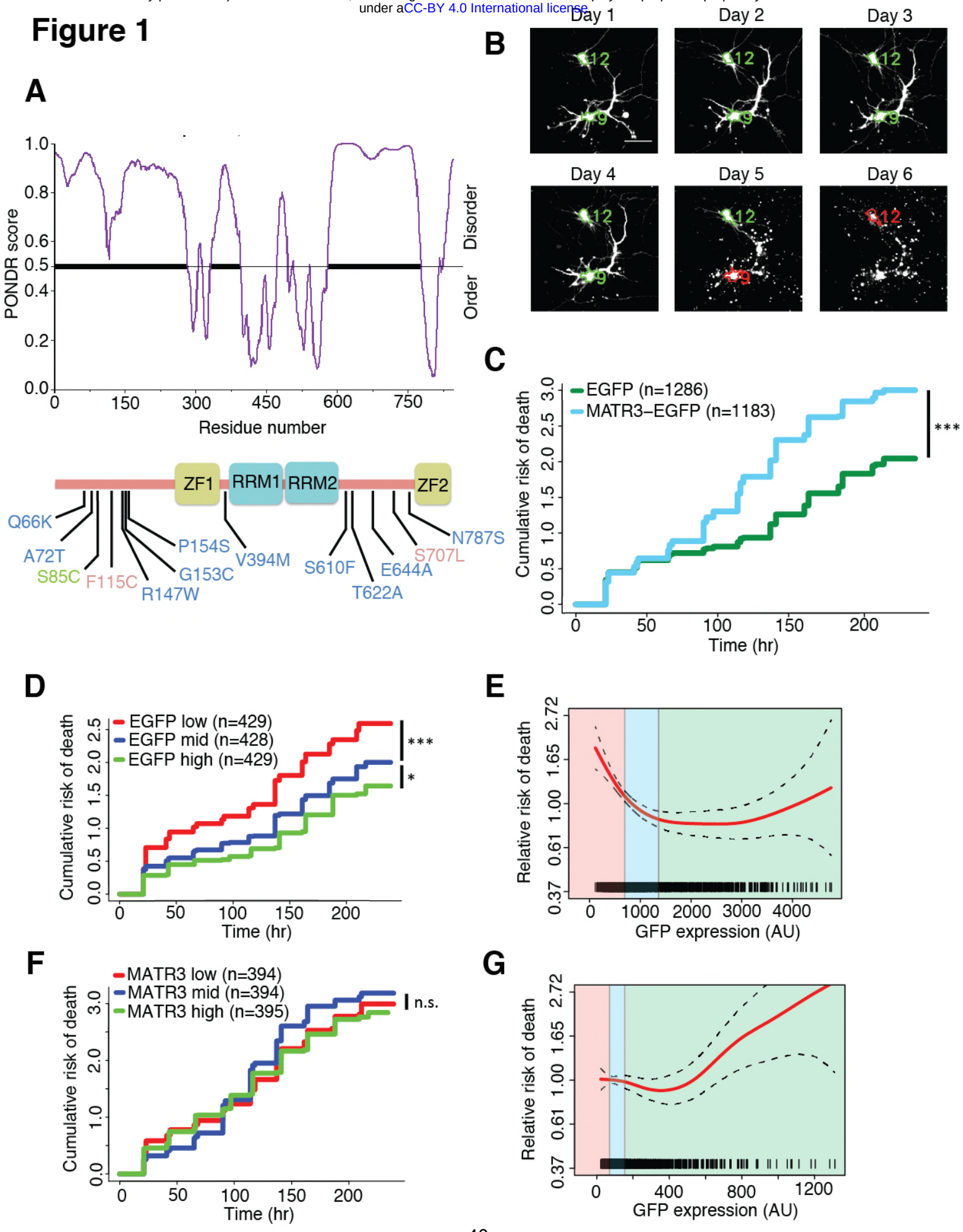

Figure 2

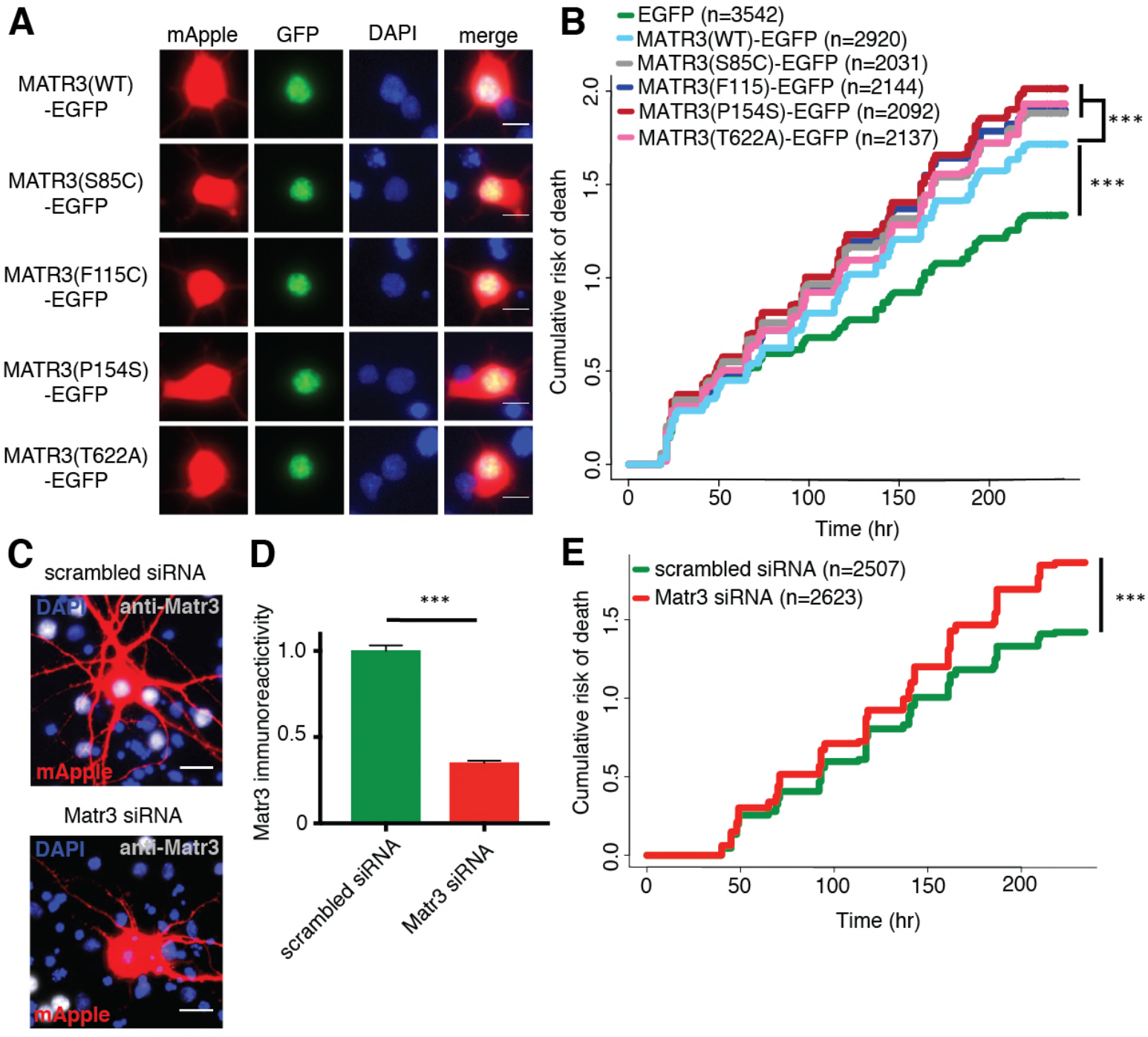

Figure 3

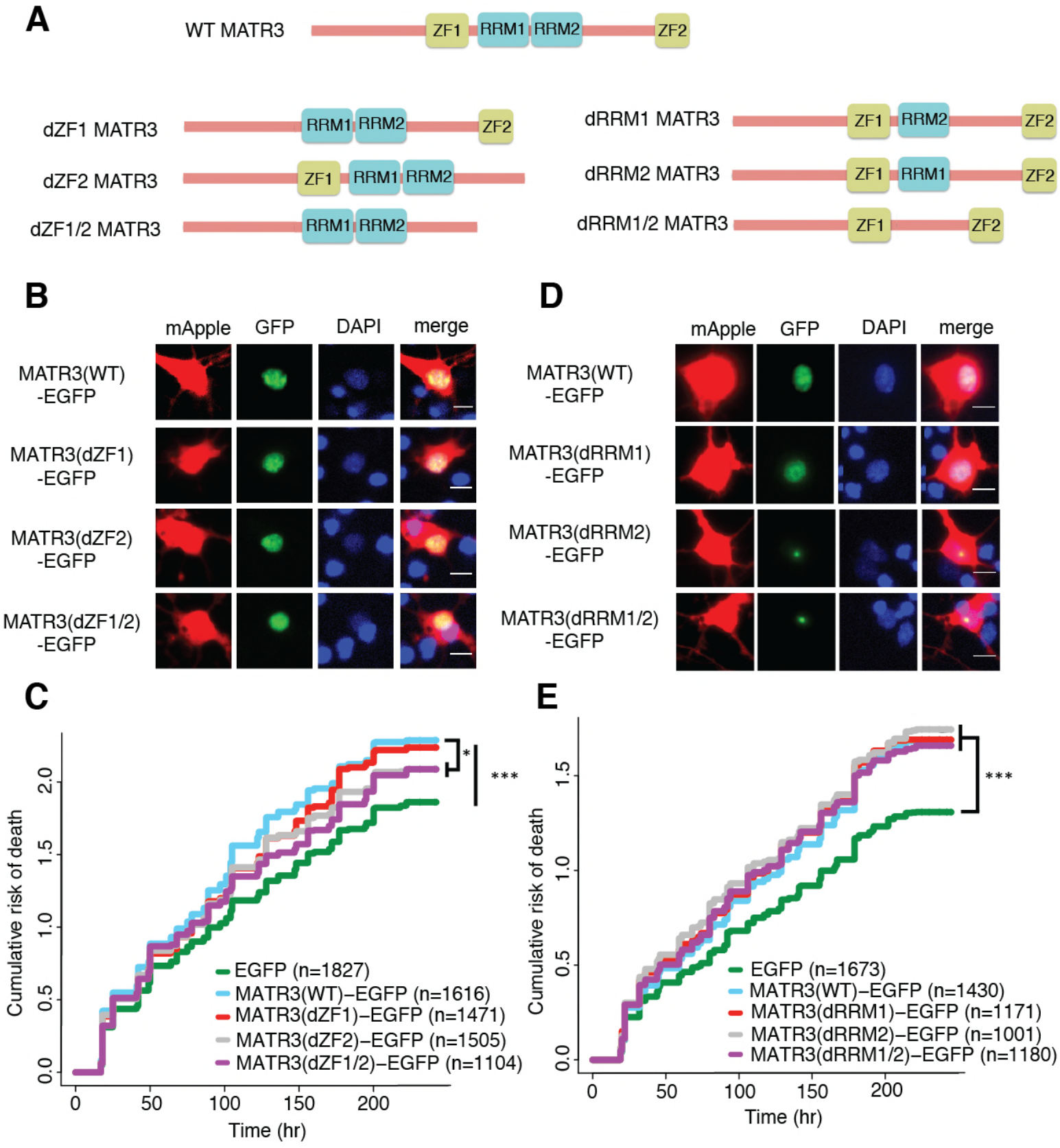

Figure 4

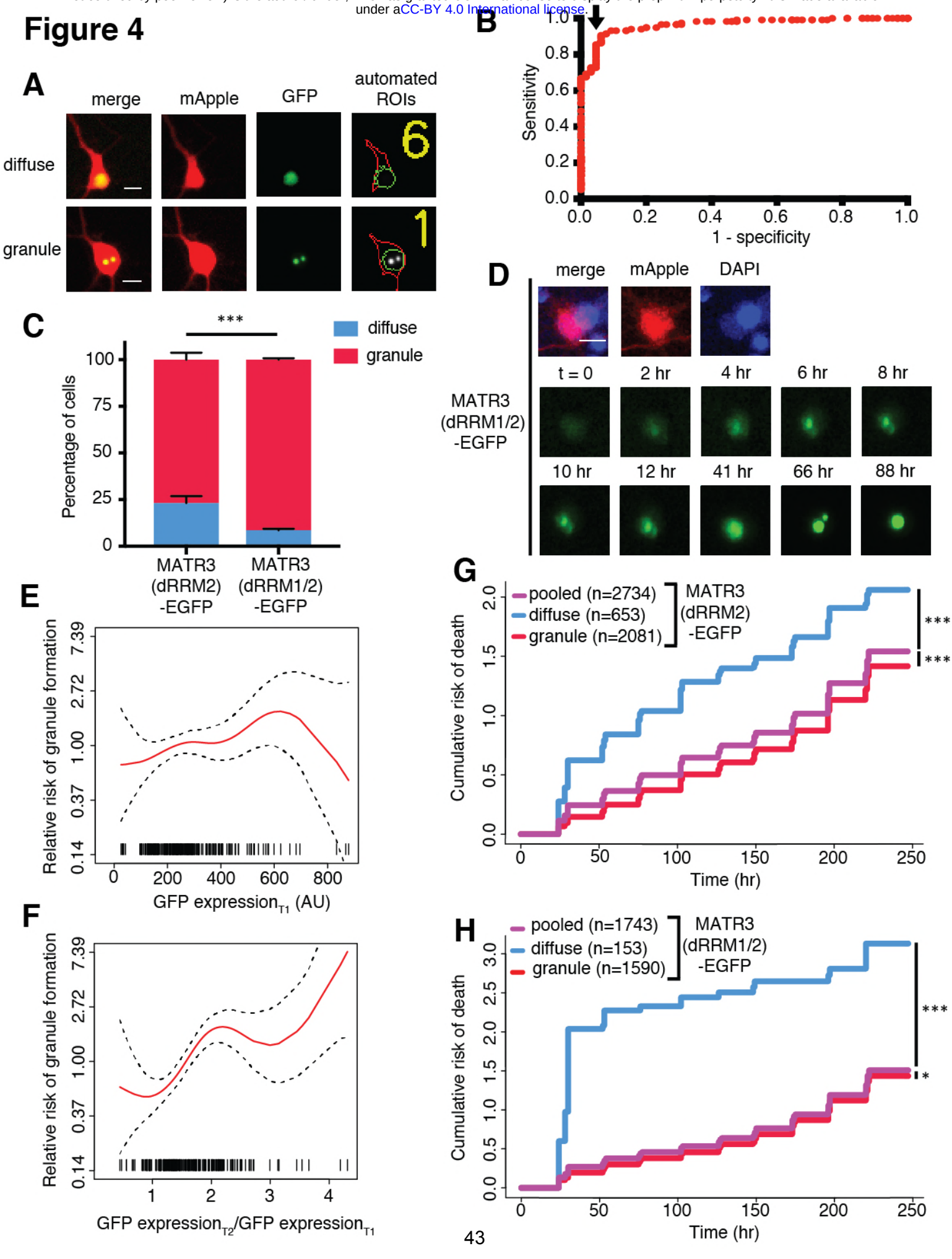

Figure 5

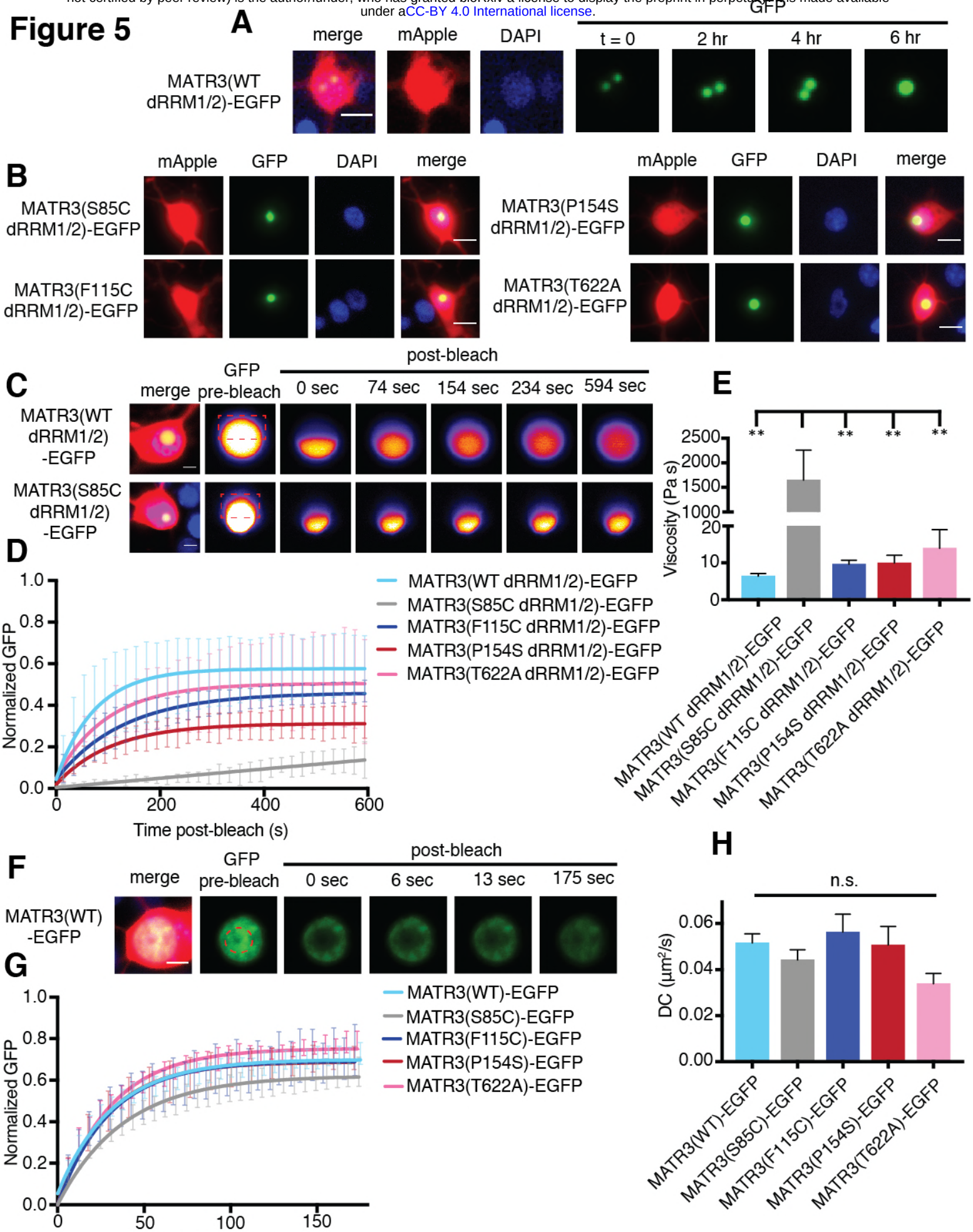

Figure 6

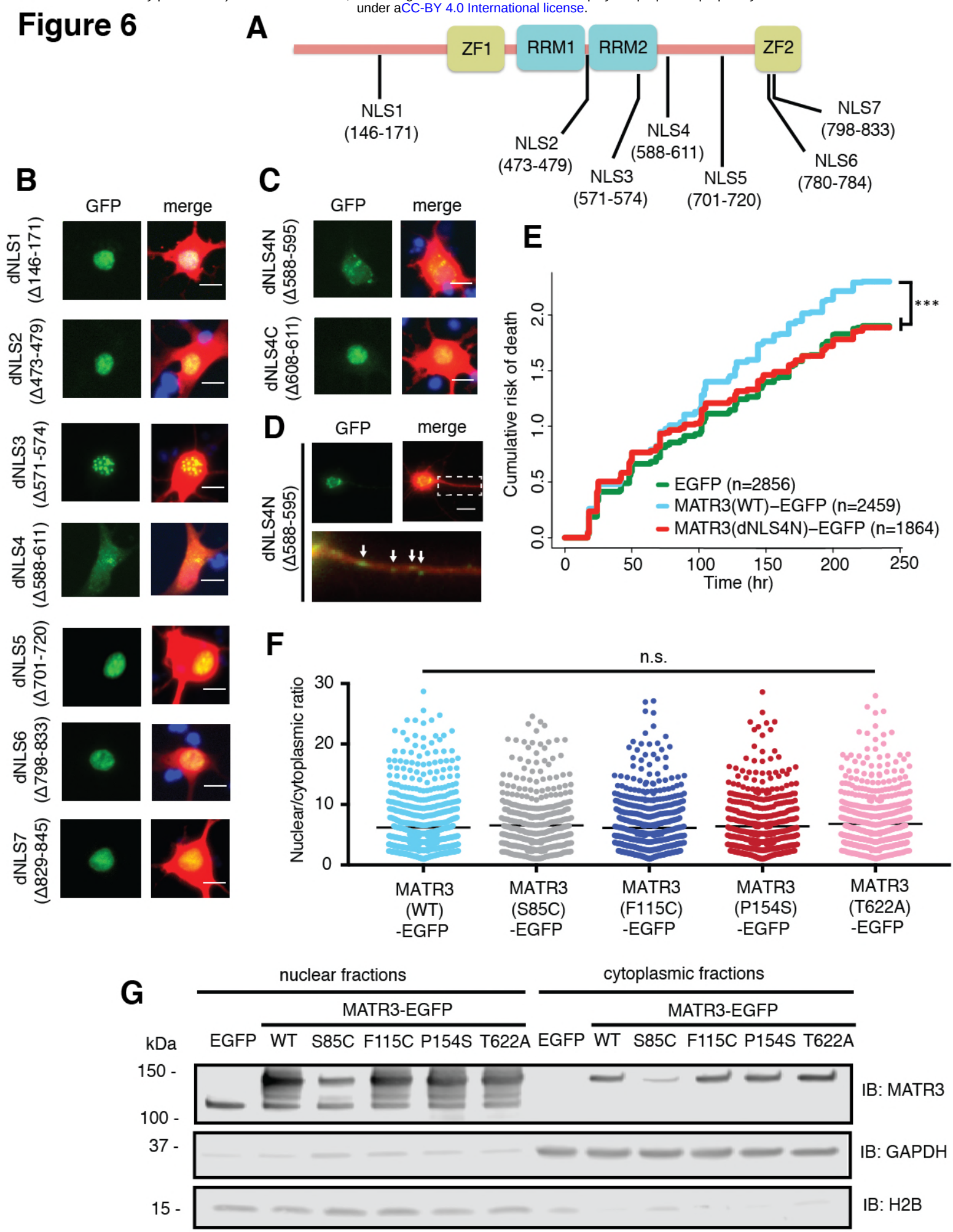

Figure 7

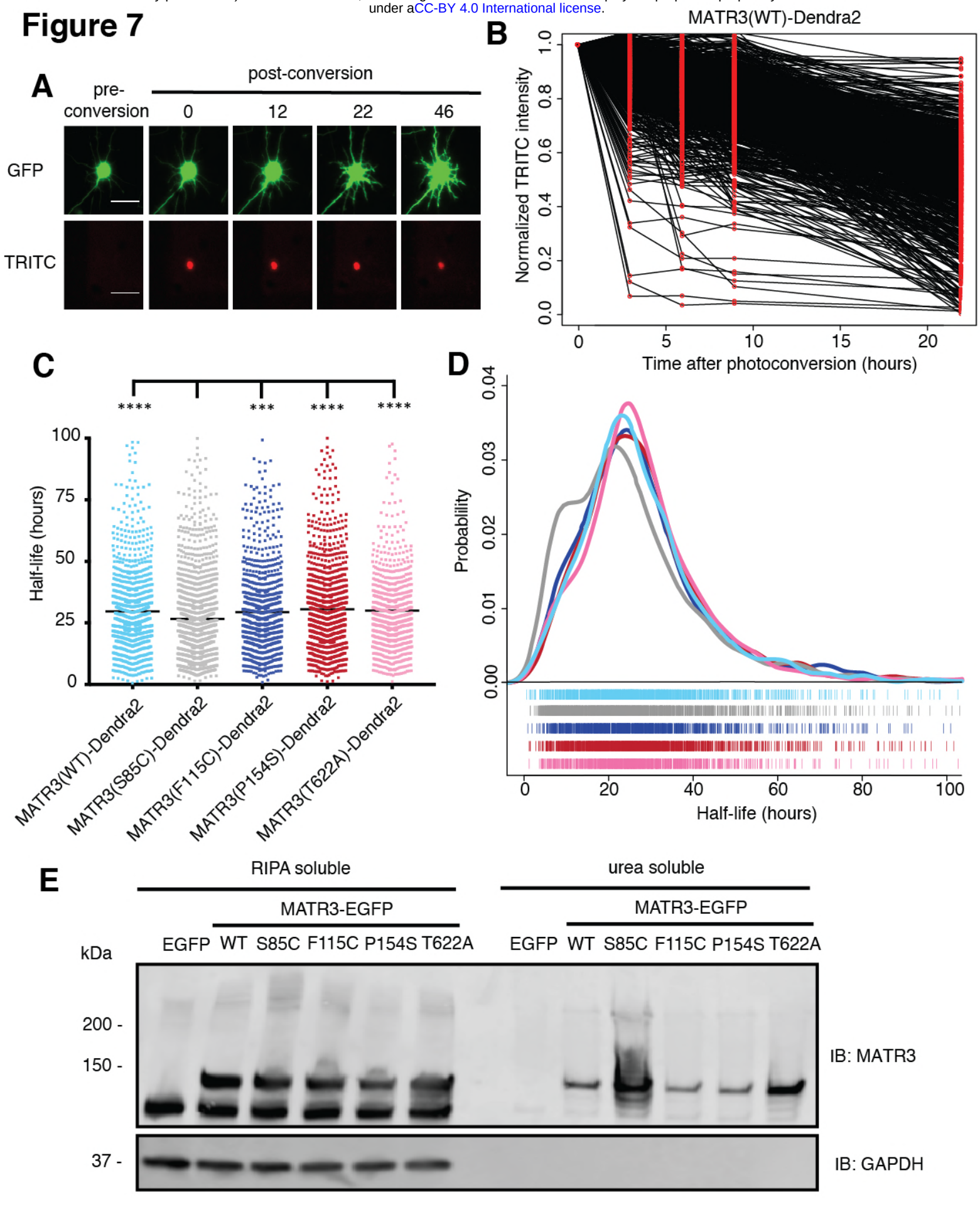

968 **FIGURE LEGENDS**

969 **Figure 1. MATR3 overexpression results in dose-dependent neurodegeneration. A.**
970 Diagram of MATR3 showing nucleic acid-binding domains as well as the distribution of
971 pathogenic mutations implicated in ALS (blue), ALS/FTD (red), and ALS/distal myopathy
972 (green) within domains predicted to be disordered by PONDR VSL2 (Peng et al., 2006).
973 **B.** Longitudinal fluorescence microscopy (LFM) allows unique identification and tracking
974 of thousands of primary neurons (green outlines) transfected with fluorescent proteins,
975 as well as monitoring of cell death (red outlines), indicated by loss of fluorescence signal
976 and changes in morphology. Scale bar, 20 μm. **C.** MATR3-EGFP expressing neurons
977 exhibited a higher risk of death compared to neurons expressing only EGFP, as
978 quantified by the hazard ratio (HR) (HR = 1.48, EGFP n = 1286, MATR3-EGFP n =
979 1183; $p < 2 \times 10^{-16}$; Cox proportional hazards). **D.** EGFP expressing cells were divided
980 into three equal groups based off expression level. Increased survival was associated
981 with higher expression levels of EGFP (comparing to medium expressers n = 428: low
982 expressers HR = 1.39, n = 429, $p = 4.2 \times 10^{-5}$; high expressers HR = 0.79, n = 429, p =
983 0.024; Cox proportional hazards). **E.** Penalized spline modeling confirmed a protective
984 effect associated with higher EGFP expression that plateaus at ~1500 arbitrary units
985 (AU); shaded colors represent low, medium and high expression ranges as in (**D**) ($p =$
986 5.3×10^{-6}; penalized spline regression). **F.** There were no significant differences in
987 survival among neurons expressing low, medium, or high levels of MATR3-EGFP
988 (comparing to medium expressers n = 394: low expressers HR = 0.99, n = 394, p = 0.94;
989 high expressers HR = 1.06, n = 395, p = 0.54; Cox proportional hazards). **G**. Similarly,
990 penalized spline analysis showed no relationship between expression and survival at low
991 and medium expression but a significant increase in risk of death with high MATR3-
992 EGFP levels (p = 0.012; penalized spline regression).
993

Figure 2. Neurons are susceptible to both gain-of-function and loss-of-function MATR3 toxicity. A. In primary rodent cortical neurons, the S85C, F115, P154S, and T622A disease-associated MATR3 mutants have the same granular nuclear distribution as MATR3(WT)-EGFP. **B.** All four disease mutations display a subtle but significant increase in toxicity compared to MATR3(WT)-EGFP (comparing to MATR3(WT)-EGFP n = 2920; MATR3(S85C)-EGFP HR = 1.16, n = 2031, $p = 3.79 \times 10^{-6}$; MATR3(F115C)-EGFP HR = 1.14, n = 2144, $p = 5.57 \times 10^{-5}$; MATR3(P154S)-EGFP HR = 1.24, n = 2092, $p = 1.77 \times 10^{-11}$; MATR3(T622A)-EGFP HR = 1.14, n = 2137, $p = 6.02 \times 10^{-5}$; Cox proportional hazards). **C-D.** siRNA targeting the endogenous rat *Matr3* reduced MATR3 antibody reactivity by approximately 65% (scrambled siRNA n = 576, anti-Matr3 siRNA n = 508, $p < 0.0001$; two-tailed t-test). **E**. Neurons transfected with anti-Matr3 siRNA displayed a higher risk of death compared to those transfected with scrambled siRNA (HR = 1.20, scrambled siRNA n = 2507, anti-Matr3 n = 2623, $p = 2.05 \times 10^{-8}$; Cox proportional hazards). Scale bars in **(A)**, 10 μm; scale bars in **(C)**, 20 μm.

Figure 3. MATR3's ZFs mediate overexpression toxicity, and its RRMs regulate subcellular distribution. A. Schematic of MATR3 domain deletion mutants. **B.** Zinc finger (ZF) domain deletions do not change the localization of MATR3-EGFP compared to the full-length protein. **C.** ZF2 deletion, either in isolation or combination with ZF1, results in modest rescue of overexpression toxicity (comparing to MATR3(WT)-EGFP n = 1616: MATR3(dZF1)-EGFP HR = 0.94, n = 1471, p = 0.10; MATR3(dZF2)-EGFP HR =0.93, n = 1505, p = 0.040; MATR3(dZF1/2)-EGFP HR = 0.90, n = 1104, p = 0.0093; Cox proportional hazards). **D.** While MATR3(dRRM1)-EGFP exhibits the same localization as MATR3(WT)-EGFP, deletion of RRM2 results in redistribution into intranuclear granules. **E.** RRM deletion had little effect on MATR3-mediated toxicity (comparing to MATR3(WT)-EGFP n = 1430: MATR3(dRRM1)-EGFP HR = 1.05, n =

1171, p = 0.25; MATR3(dRRM2)-EGFP HR = 1.09, n = 1001, p = 0.066; MATR3(dRRM1/2)-EGFP HR = 1.04, n = 1180, p = 0.42). Scale bars in **(B)** and **(D)**, 10 µm.

Figure 4. MATR3(dRRM2)-EGFP and MATR3(dRRM1/2)-EGFP are highly neurotoxic in their diffuse form. A. Automated analysis of MATR3-EGFP distribution in transfected primary cortical neurons. Regions of interest (ROIs) were drawn around the cell body (marked by mApple fluorescence, red) and diffuse MATR3-EGFP (indicated by GFP fluorescence, green), and used to calculate a coefficient of variation (CV) representing MATR3-EGFP distribution within each ROI. **B**. Receiver operating characteristic (ROC) curve for MATR3-EGFP CV values. A CV threshold of 0.92 (arrow) identified cells with intranuclear MATR3-EGFP granules with 87.2% sensitivity and 93.9% specificity. **C.** Using this cutoff, we determined that 1 day after transfection, 23.4% (653/2734) of MATR3(dRRM2)-EGFP neurons displayed intranuclear granules compared to only 8.8% (153/1743) of MATR3(dRRM1/2)-EGFP cells. ($p < 0.00001$; Fisher's exact test). **D.** Intranuclear granules form in a time-dependent manner in neurons expressing MATR3(dRRM2)-EGFP and MATR3(dRRM1/2)-EGFP. **E-F.** Penalized spline models depicting the relationship between MATR3(dRRM2)-EGFP expression on day 1 (**E**) or change in GFP expression between day 1 and day 2 (**F**), and risk of developing an intranuclear granule by day 3. Expression level at day 1 was not significantly associated with risk of granule formation (**E**; p = 0.30; penalized spline regression), but the relative increase in expression from day 1 to day 2 is (**F**; p = 0.015; penalized spline regression). **G.** For MATR3(dRRM2)-EGFP, neurons exhibiting granules by day 1 displayed improved survival compared to the pooled combination of all cells. Conversely, neurons with diffusely distributed MATR3(dRRM2)-EGFP fared far worse (comparing to the pooled condition: cells with granules n = 2081, HR = 0.86, $p = 1.02 \times 10^{-5}$; cells with

diffuse protein n = 653, HR = 1.75, $p < 2 \times 10^{-16}$; Cox proportional hazards). **H.** Neurons with MATR3(dRRM1/2)-EGFP granules by day 1 similarly displayed a reduced risk of death in comparison to the pooled group, while diffuse MATR3(dRRM1/2)-EGFP was highly toxic (comparing to the pooled condition: cells with granules n = 1590, HR = 0.92, p = 0.03; cells with diffuse protein n = 153, HR = 3.78, $p = 2 \times 10^{-16}$; Cox proportional hazards). Scale bars in **(A)** and **(B)**, 10 μm.

Figure 5. MATR3(dRRM1/2)-EGFP droplets display liquid-like properties that are affected by the S85C mutation. A. MATR3(dRRM1/2)-EGFP and MATR3(dRRM1/2)-EGFP droplets show liquid-like properties such as mobility and fusion. **B.** Pathogenic MATR3 mutations on the dRRM1/2 background result in similar phase-separated droplets. **C-D.** Fluorescence recovery after photobleaching (FRAP) of MATR3(dRRM1/2)-EGFP droplets shows internal rearrangement consistent with liquid-like behavior, but the recovery of MATR3(S85C dRRM1/2)-EGFP droplets was significantly delayed. **E.** MATR3(S85C dRRM1/2)-EGFP droplets displayed significantly higher viscosity in comparison to other variants (comparing to S85C MATR3(dRRM1/2)-EGFP n = 5: WT MATR3(dRRM1/2)-EGFP n = 5, p = 0.0045; F115C MATR3(dRRM1/2)-EGFP n = 5, p = 0.0046; P154S MATR3(dRRM1/2)-EGFP n = 5, p = 0.0046; T622A MATR3(dRRM1/2)-EGFP n = 4, p = 0.0079; one-way ANOVA with Tukey's post-hoc test). **F-G.** FRAP experiments involving full-length MATR3-EGFP variants showed no differences in rates of return. **H.** Similarly, there were no differences in diffusion coefficients (DC) among full-length MATR3 variants (MATR3(WT)-EGFP n = 5, MATR3(S85C)-EGFP n = 5, MATR3(F115C)-EGFP n = 5, MATR3(P154S)-EGFP n = 5, MATR3(T622A)-EGFP n = 4); p = 0.17; one-way ANOVA). Scale bars in **(A)** and **(B)**, 10 μm; scale bars in **(C)** and **(F)**, 5 μm.

Figure 6. Reducing MATR3 nuclear localization mitigates overexpression toxicity. **A.** Schematic showing putative MATR3 nuclear localization signals (NLS). **B-C.** Deletion of the N-terminal arm of NLS4 (dNLS4N) led to nuclear MATR3 clearance in neurons. **D.** MATR3(dNLS4N)-EGFP forms granular structures in the cytoplasm and neuronal processes (white arrows). **E.** Disrupting nuclear localization of MATR3 prevents neurotoxicity from overexpression (MATR3(WT)-EGFP n = 2459; MATR3(dNLS4N)-EGFP n = 1864, HR = 0.89, p = 0.00041; Cox proportional hazards). **F-G.** Pathogenic MATR3 mutants display no difference in subcellular protein localization as assessed by automated image nuclear/cytoplasmic analysis (**F**; MATR3(WT)-EGFP n = 824, MATR3(S85C)-EGFP n = 499, MATR3(F115C)-EGFP n = 634, MATR3(P154S)-EGFP n = 554, MATR3(T622A)-EGFP n = 677; p = 0.067; one-way ANOVA) or biochemical fractionation in transfected HEK293T cells (**G**). Nevertheless, Western blot demonstrated reduced abundance of the S85C mutant in transfected HEK293T cells. Scale bars in **(B)** and **(C)**, 10 μm; scale bar in (D), 50 μm.

Figure 7. Pathogenic MATR3 mutations have little effect on MATR3 turnover, but a subset reduce solubility. A. Optical pulse labeling of Dendra2-tagged MATR3 variants. Each neuron is transfected with EGFP alone to outline the cell body, as well as MATR3-Dendra2, which fluoresces in the red channel (TRITC) upon photoconversion. Scale bar, 50 μm. **B.** Normalized red fluorescence (TRITC) signal for individual neurons. The time-dependent decay of red fluorescence over time is used to calculate MATR3-Dendra2 half-life for each neuron. **C-D.** MATR3(S85C)-Dendra2 displayed a subtle but significant reduction in half-life compared to MATR3(WT)-Dendra2 and the other pathogenic mutants tested (comparing to MATR3(S85C)-Dendra2 n = 1670: MATR3(WT)-Dendra2, n = 1269, p < 0.0001; MATR3(F115C)-Dendra2, n = 1122, p = 0.0001; MATR3(P154S)-

Dendra2, n = 1509, $p < 0.0001$; MATR3(T622A)-Dendra2, n = 923, $p < 0.0001$; one-way ANOVA with Tukey's post-hoc test). **E.** Sonication in RIPA resulted in equivalent amounts of all MATR3 variants by Western blotting. The S85C variant was markedly enriched in the RIPA-insoluble, urea-soluble fraction, while the T622A variant showed more modest enrichment.